Delamination analysis of a ductile phase-toughened environmental barrier coating for oxygen-rich turbopumps

Isha Gupta [a], Spencer V. Taylor [a], Christopher M. Kiel [b], Andres Garcia-Jimenez [a], Zachary C. Cordero [a,*]

[a] *Aeronautics and Astronautics, Massachusetts Institute of Technology, Cambridge, MA 02139, United States of America*
[b] *Materials Science and Engineering, Massachusetts Institute of Technology, Cambridge, MA 02139, United States of America*

ARTICLE INFO

ABSTRACT

The turbine in an oxygen-rich turbopump subjects materials to high-pressure gaseous oxygen environments, where the risk of metal fires presents a potentially catastrophic failure mode. A candidate approach for mitigating particle impact ignition, one key metal ignition mechanism, is to coat metallic components with an inert ceramic environmental barrier coating; however, such coatings are susceptible to delamination during the rapid thermal transients upon engine startup and shutdown. Here, we investigate the delamination risk of a ductile phase-toughened composite environmental barrier coating under a nominal flight cycle of a reusable boost-stage rocket engine. The coating of present interest comprises a borate-based glass-ceramic matrix reinforced with Ni and is applied as an aqueous slurry that bonds to the substrate upon firing. We first varied the Ni content in the coating and characterized its structure, finding that the Ni reinforcement sinters to the substrate and percolates through the brittle glass-ceramic when the Ni volume fraction exceeds 0.3, in excellent agreement with percolation theory. We also experimentally assessed the thermomechanical properties of the coating and used these measurements to compute its energy release rate under the thermal transients expected in service. Our analysis shows that thermal stresses and energy release rates are greatest during engine startup and shutdown, with energy release rates on the order of 100 J/m^2 for a 100-μm thick coating on an IN718 substrate. Our analysis then highlights strategies for reducing the energy release rate, which include tailoring the thermal expansion coefficient to balance transient vs. steady-state thermal stresses and using active heating to promote film boiling upon exposure to cryogenic liquid oxygen, thus mitigating the severity of cold shocks. Most importantly with respect to materials design, we predict that interpenetrating composite coatings with Ni concentrations greater than 0.3 exhibit enhanced toughness via crack bridging, allowing them to resist delamination under even the most aggressive operating conditions. These results highlight the potential of high-toughness metal/ceramic interpenetrating composite coatings in thermal and environmental protection applications where extreme thermal transients delaminate conventional monolithic ceramic coatings.

1. Introduction

In the oxygen-rich turbopump of oxidizer-rich and full-flow staged combustion rocket engines, a high-temperature, oxygen-rich gas flows from the preburner into the turbine, where turbine inlet temperatures and O$_2$ partial pressures are in the range 470–770 K and 150–600 bar [1–3], respectively. Under these conditions, conventional turbines made from high-strength Ni-base superalloys with high concentrations of reactive Ti and Al are susceptible to metal ignition and burning [4]. Metal ignition has been linked to several high-profile launch failures

including those of Sea Launch NSS8 and Antares Orb-3, and there are ongoing efforts to identify and mitigate sources of metal ignition [3,5,6].

A key metal ignition mechanism is particle impact ignition, where small particles entrained within the internal gas stream impact engine components such as turbine rotors at high velocities. The resulting localized heating causes the particle to ignite and kindle beyond the impacted area, leading to a macroscale metal fire. A potential method to protect turbines against particle impact ignition is to coat them with inert, oxygen-compatible environmental barrier coatings (ox-EBCs). Currently, inert ceramic coatings are widely used in aeroengines for

thermal and environmental protection. However, these coatings are challenging to implement in rocket engine turbomachinery where they face a greater risk of delamination due to thermal stresses from the rapid thermal transients on engine startup and shutdown [7]. Compared to an aeroengine turbine, the turbine in an oxygen-rich turbopump sees a smaller temperature change during startup and shutdown, typically from cryogenic temperatures to 770 K, but over a much shorter time (specifically, hundreds of milliseconds in a rocket engine versus minutes in an aeroengine) and with higher heat transfer coefficients [7,8]. Taken together, these conditions give rise to steep thermal gradients that drive high thermal stresses and promote coating delamination. Coating delamination, beyond exposing the underlying substrate to the oxygen-rich environment, can cause loose ox-EBC fragments to flow downstream to critical engine components, where they can block injector orifices or trigger particle impact ignition at other locations. These delamination risks are especially critical given recent interest in rocket engine reusability, where coatings must survive multiple restarts over tens of flights before engine retirement or overhaul. For this reason, the delamination behavior of ox-EBCs under thermal transients must be further examined before they can be safely implemented in reusable rocket engines.

Previous studies have assessed general modes of coating delamination under thermal transients [9,10], noting that the dominant delamination mechanism depends on the nature of in-plane stresses. During cold shock, where the coating is rapidly exposed to low temperatures, coatings typically experience tensile stresses, and edge-delamination from through-thickness channel cracks is the dominant mechanism [11]. By contrast, during hot shock, coatings generally experience compressive stresses which drive interfacial buckling delamination above internal cracks. Buckling delamination is further promoted by adiabatic cracking which inhibits heat flow and increases the temperature gradient across the crack faces [9].

Considering that delamination mechanisms are temperature-dependent, one option to inhibit delamination is by modifying engine operating conditions. For instance, several studies found that for thermal barrier coatings (TBCs) in aeroengines, managing the cooling trajectory during engine shutdown can prevent delamination by reducing the energy release rate, which serves as the driving force for delamination, below the toughness of the coating/substrate interface [12–16]. Although these studies focused on the thermal transients in aeroengines, which differ from those in rocket engines as previously discussed, their thermomechanical analysis frameworks and mitigation approaches are valuable to our current study of ox-EBCs in rocket engines.

Additionally, previous works discuss coating and material design approaches for preventing delamination [12,15,16]. They describe, for instance, that the energy release rate generally scales with coating thickness, suggesting that thinner coatings can survive more drastic thermal transients [12,15]. Further, delamination behavior depends on the ratio of the thermal transient timescale to the heat diffusion timescale, $\frac{t_c}{t_d}$, where $t_d = \frac{w^2}{D}$ with w as the thickness of the coated substrate and D as thermal diffusivity. When $\frac{t_c}{t_d} \gg 1$, the system approaches steady-state behavior and coating stresses scale with $E_c(\alpha_c - \alpha_{sub})\Delta T_c$, where E_c is the Young's modulus of the coating, α_c and α_{sub} are the coefficients of thermal expansion (CTEs) of the coating and substrate, respectively, and ΔT_c is the difference between the current temperature and the stress-free temperature of the coating. Alternatively, when $\frac{t_c}{t_d} \ll 1$, thermal gradients within the coating give rise to an additional in-plane coating stress which generally scales with $E_c\alpha_c(T_c - T_{sub})$, where T_c and T_{sub} are the coating and the substrate temperature, respectively [15,16]. Thus, under steady-state thermal conditions, minimizing CTE mismatch between the coating and substrate minimizes thermal stresses; by contrast, under rapid thermal transients, minimizing CTE of the coating can minimize thermal stresses. Considering that an oxygen-rich turbine experiences a combination of these scenarios, it is necessary to optimize coating parameters and properties against both steady-state and
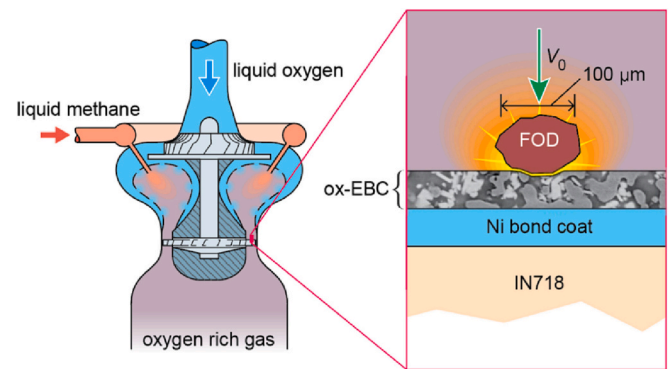

Fig. 1. Oxygen-rich turbopump with inset showing particle impact of a turbine blade coated with the ox-EBC of present interest.

transient thermal stresses.

Considering the framework outlined by these delamination prevention strategies, one emerging composite ox-EBC system shows promise for use in reusable rocket engines [17]. This ox-EBC, shown schematically in Fig. 1, comprises barium-aluminoborate glass, a refractory oxide, and nominally pure Ni [18]. The inert glass-ceramic combination provides oxidation and ignition resistance typical of conventional ceramic coatings, while the Ni phase enhances the durability of the coating via ductile-phase toughening. Preliminary experiments suggest that this composite coating can prevent particle impact ignition in high-pressure O_2 environments and can withstand 50 thermal cycles between temperatures of 20 °C and 900 °C [17]. However, exact time-temperature profiles and heat flux conditions were not reported, and it is unclear whether these previous experiments captured the extreme thermal transients seen in reusable staged-combustion rocket engines where the engine restarts four times during a single flight. Thus, the detailed thermomechanical response of the ox-EBC and its susceptibility to delamination under reusable rocket engine working conditions have not been explicitly quantified.

In this study, we analyze the thermomechanical delamination behaviors of the composite ox-EBC mentioned above under the thermal transients of an oxygen-rich turbopump in a reusable boost-stage engine [19]. First, we describe the synthesis process of the composite ox-EBC and characterize the resulting microstructure and thermomechanical properties. We then combine heat transfer analysis with linear elastic fracture mechanics to predict temperatures, thermal stresses, and energy release rate for delamination under the given thermal transients. Finally, we explore strategies to mitigate the risk of delamination by optimizing the coating properties and composite architecture. The insights from this work can more broadly serve as a framework to guide the design of high-toughness composite coatings for thermal and environmental protection.

2. ox-EBC synthesis and characterization

We prepared the composite ox-EBC in bulk form and as a coating according to rough guidelines outlined in previous work [17]. First, we formed a powder base by jar milling a combination of BaO, CeO_2, B_2O_3, and Al_2O_3 powders with the overall weight fractions given in Table 1.

Table 1
Composition of slurry used to synthesize the ox-EBC.

Constituent	wt.%
Ni	47.7
BaO	17.8
CeO_2	16.8
B_2O_3	10.1
Al_2O_3	7.6

Fig. 2. Macrograph of a IN718 blisk with a Ni bond coat, a green ox-EBC, and a sintered ox-EBC. (For interpretation of the references to colour in this figure legend, the reader is referred to the web version of this article.)

After jar milling for 24 h, we added the Ni powder and jar milled for an additional 5 h. To prepare bulk specimens, we pressed the milled powder base into cylindrical pellets and sintered the pellets in an inert Ar atmosphere, heating at 10 K/min from room temperature to 1323 K, holding at 1323 K for 30 min, and then furnace cooling to room temperature. The pellets exhibited a linear shrinkage of 15% during sintering. To prepare coatings from the milled powder, we first grit blasted thin IN718 disks. We then prepared an aqueous slurry comprising one part milled powder to three parts water by mass and dipped the substrates in the slurry. We let the dipped substrates dry in air and sintered the dried substrates according to the heating schedule described above. Coatings with thicknesses greater than 20 μm often cracked due to shrinkage during sintering. As a result, coating cycles were repeated to achieve a desired coating thickness.

The coating process is outlined in Fig. 2, which shows an additively manufactured IN718 blisk substrate at each step: first, as-received with a Ni bond coat; second, after dipping and drying with a green ox-EBC top coat; and finally, after firing with a sintered ox-EBC. A cross-section of the ox-EBC in coating form on a bare IN718 substrate reveals three distinct phases, as labeled in Fig. 3. Using energy-dispersive X-ray spectroscopy, we identified two of the phases as Ni and $CeBO_3$. Fig. 4 shows X-ray diffraction measurements of the coating, where the lack of additional Bragg peaks together with glass composition data from previous studies indicate that the third phase is barium-aluminoborate glass [20,21]. The volume fractions of Ni and $CeBO_3$ in this coating, determined through stereological measurements, are 0.35 and 0.15, respectively. Assuming that the density of barium-aluminoborate glass is 3.25 g/cm^3 [22], the corresponding weight fractions of Ni and $CeBO_3$ are

0.50 and 0.14. These values match the weight fractions of Ni and CeO_2 powders included in the mixed powder base (0.48 and 0.17), suggesting that Ni does not react with the oxide constituents during sintering while, separately, the CeO_2 is converted to $CeBO_3$. Through linear intercept measurements, we observe that the resulting characteristic width of the Ni phase is 4 μm with mean spacing of 10 μm, and the mean diameter of the $CeBO_3$ particles is 2 μm. While the coating itself had negligible porosity, grain boundary pores in the IN718 substrate formed due to a reaction between the oxide constituents in the coating and Cr and Nb in the IN718 substrate. These reactions can be suppressed by incorporating a pure Ni bond coat between the coating and the substrate.

To identify key thermal phase transitions that may limit the operating temperature of the coating, we performed differential scanning calorimetry and dilatometry in an inert argon atmosphere with heating rates of 20 K/min and 10 K/min, respectively. The thermogram shown in Fig. 5a reveals a glass transition temperature T_g of 830 K (also confirmed by the dilatometry results in Fig. 5b), a crystallization temperature T_x of 1025 K, and a liquidus temperature T_L of 1120 K. Our measured T_g and T_x match those previously reported for barium-aluminoborate glasses [21,23], further confirming the identity of the glass phase. The maximum sintering temperature of 1323 K well exceeds the measured T_L, suggesting that the oxide constituents react to form liquid during sintering. We also find that T_g, which sets the maximum operating temperature of the coating, is only 60 K higher than that of the turbine
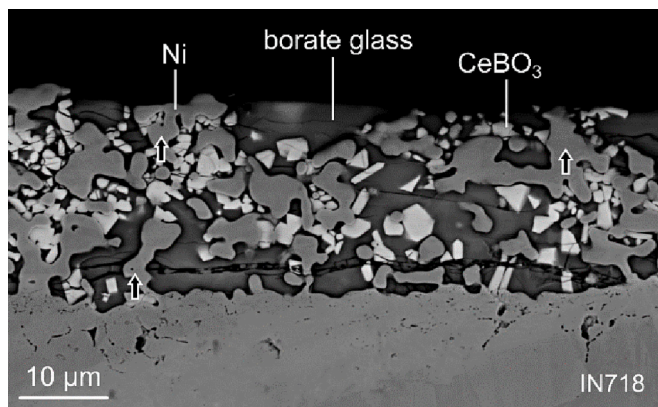

Fig. 3. SEM micrograph of an ox-EBC coating with a Ni volume fraction of 0.35 deposited on an IN718 substrate. Arrows indicate Ni ligaments that bridge cracks in the brittle glass-ceramic.
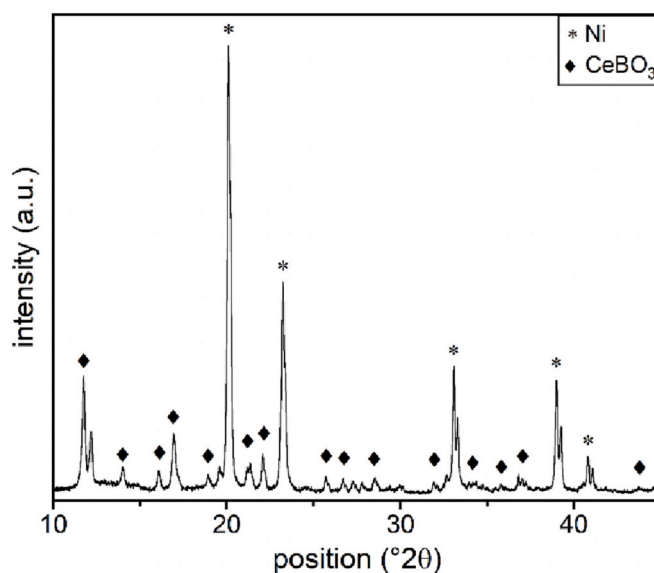

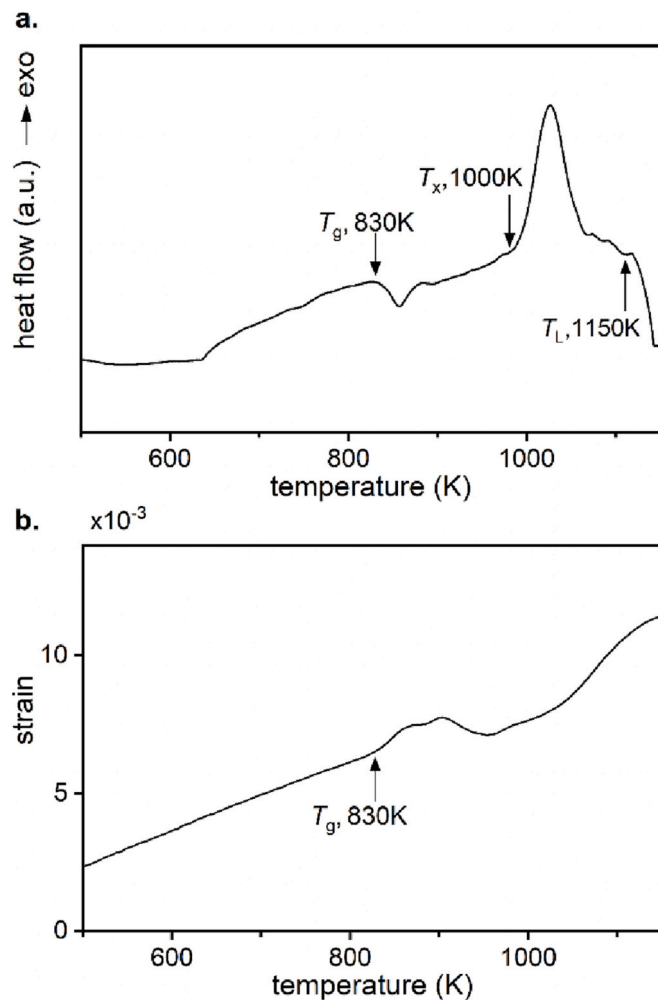**Fig. 4.** XRD diffractogram from a bulk ox-EBC sample.

Fig. 5. (a) Differential scanning calorimetry on a bulk ox-EBC specimen, showing glass transition (T_g), crystallization (T_x), and liquidus (T_L) temperatures of the barium-aluminoborate glass phase. (b) Dilatometry measurements which also show $T_g = 830$ K.

Fig. 6. Thermal conductivity (k_{ox}) of bulk samples of ox-EBC (shown by circles) versus the Ni volume fraction ($V_{f,Ni}$). The data deviate from the lower bound above $V_{f,Ni} \approx 0.25$, indicating percolation of the conductive Ni phase near this composition. The curves represent the predicted Hashin-Shtrikman bounds on the ox-EBC thermal conductivity.

inlet temperature of the RD-170, a representative oxygen-rich turbo-pump [2].

With this initial insight into coating structure and thermal properties, we predict that the inert glass-ceramic phase protects against ignition in high-pressure O_2 and mitigates particle impact damage while the ductile Ni phase reinforces the ox-EBC to protect against fracture and delamination. To achieve an optimal combination of these behaviors, we investigated the effects of Ni volume fraction on the ox-EBC thermal properties, microstructure, and mechanical properties. We first measured the thermal diffusivity of bulk samples using laser flash measurements over the temperature range 300 K to T_g. We assessed samples of pure Ni, pure glass-ceramic, and ox-EBC with Ni volume fraction $V_{f,Ni}$ in the range 0.10 to 0.35. To prepare these samples, we adjusted the relative weight fraction of Ni within our base powder (Table 1), resulting in the desired Ni volume fraction. We then pressed these powders into cylindrical pellets and sintered according to the heating schedule described earlier in this section. By obtaining the average thermal diffusivity over the temperature range and assuming a volumetric heat capacity ρC_p of 4 MJ/m³-K, we measured the thermal conductivity values summarized in Fig. 6, where we see that the thermal conductivity increases with increasing Ni content. The solid curves in Fig. 6 represent the Hashin-Shtrikman bounds on thermal conductivity calculated using the measured values for the monolithic glass-ceramic and pure Ni.
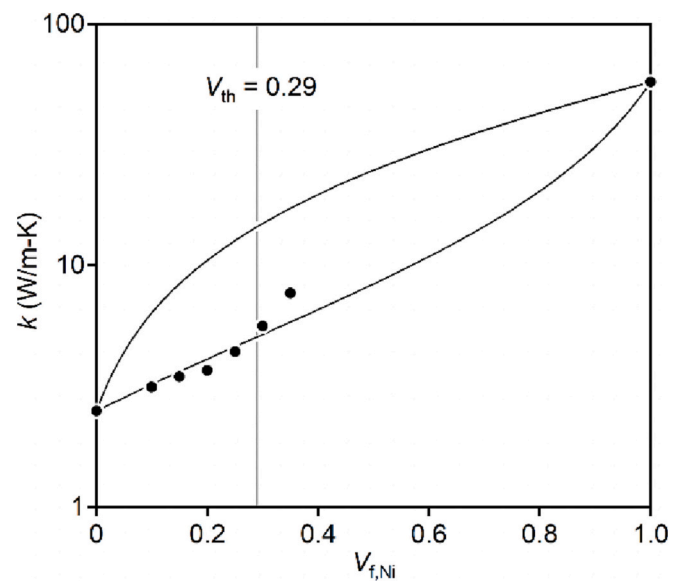
Notably, the measured thermal conductivity in Fig. 6 increases more rapidly with $V_{f,Ni}$ above roughly 0.25. To examine the microstructural cause of this behavior, we selectively etched the barium-aluminoborate glass from the ox-EBC pellets using concentrated aqueous $FeCl_3$. We found that for samples with $V_{f,Ni} \leq 0.25$, etching and removal of the glass phase also dislodged the Ni phase, and the surface of the sample contained both glass and Ni after etching, as shown in Fig. 7a. For samples with $V_{f,Ni} = 0.25$, we found localized Ni clusters (Fig. 7b), likely connected via weaker links but still not allowing a self-supporting Ni structure in the absence of the glass phase. By contrast, samples with $V_{f,Ni} \geq 0.3$ revealed a self-supporting Ni scaffold upon removal of the glass phase, indicating that Ni forms a percolating network through the ox-EBC (Fig. 7c). Several studies have explored the phenomenon of phase percolation in a heterogeneous material [24–27]. For instance, Torquato et al. [25] applied the theory of random overlapping spheres to study percolation in a sintered material system, showing that for penetrable spheres above a volume fraction of $V_{th} = 0.29$, called the percolation threshold, the individual particles cluster together to form a continuous network in an infinitely large system. Given that the characteristic length of our bulk samples (5 mm) is significantly larger than that of the spherical Ni particles in the unsintered material (3 μm), the results in Fig. 7 show that the transition from disconnected Ni particles to a percolating Ni structure between $V_{f,Ni} = 0.25$ to 0.3 is well predicted by the theoretical percolation threshold of $V_{f,Ni} = 0.29$ for an infinitely large system. Considering the thermal conductivity data in Fig. 6, this percolation transition between $V_{f,Ni} = 0.25$ to 0.3 causes the rapid increase in thermal conductivity above the theoretical percolation threshold. We also note that the percolation threshold scales with the characteristic length of the system L as $V_{th}(L)$ - $V_{th}(L = \infty) \propto L^{-\frac{1}{\nu}}$, where $\nu = 0.88$ [26]. Thus, the ox-EBC may have a slightly higher percolation threshold in coating form than observed above for the bulk pellets.

Percolation of Ni in the ox-EBC significantly impacts its fracture and delamination behaviors [28,29]. Due to a CTE mismatch between constituents, thermal stresses develop in the ox-EBC during post-sinter cooling, causing cracks to form in the brittle glass-ceramic. These cracks are then bridged by the percolating ductile Ni phase, as highlighted by the arrows in Fig. 3, which inhibits further crack propagation. We also see that cracks within the glass phase deflect into the glass/Ni
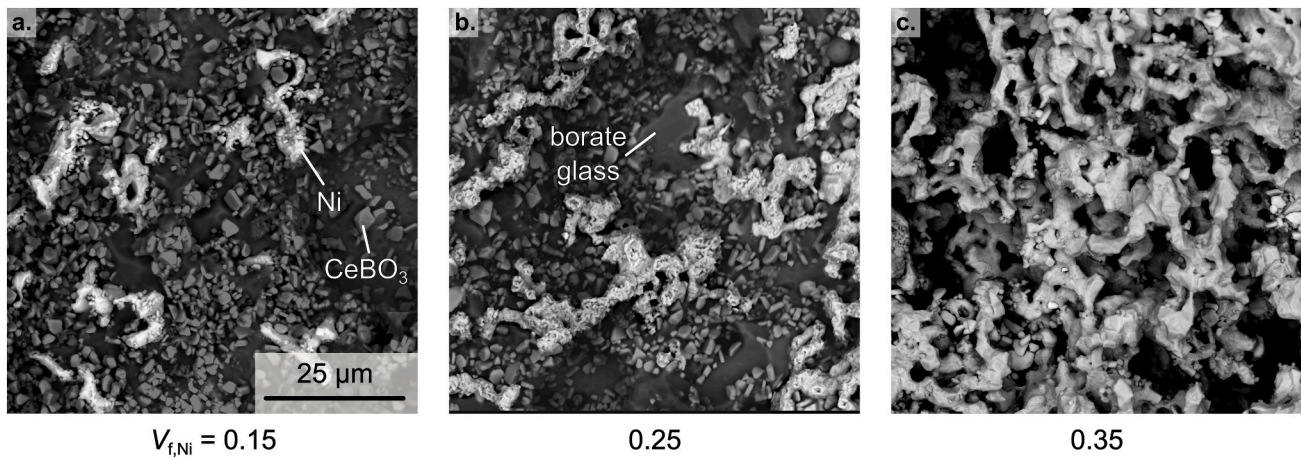
Fig. 7. SEM images of bulk ox-EBC specimens after selective etching of the glass phase. The sample with $V_{f,Ni} = 0.35$ retains a self-supporting Ni skeleton after etching, demonstrating Ni percolation. Contrast has been manually edited for clarity.

interface, suggesting that the composite structure increases crack tortuosity and thus hinders crack propagation. Through these toughening mechanisms, the Ni structure in the ox-EBC serves a role similar to the ductile reinforcement phases within traditional brittle-matrix composites which serve to improve toughness [30–33]. Additionally, the percolating Ni phase bonds directly with the substrate, creating a strong interface that enhances coating delamination resistance.

We also measured several mechanical properties of the ox-EBC. We characterized Young's modulus using ultrasonic time-of-flight measurements on bulk ox-EBC samples with varying Ni content. These measurements assumed a Poisson's ratio of 0.3. The results and the Hashin-Shtrikman bounds (shown as solid lines) are summarized in Fig. 8. The measured values in the range $V_{f,Ni} = 0.1$ to 0.35 generally fall within the Hashin-Shtrikman bounds, with some exceptions which we attribute to porosity effects. The average of the two bounds, indicated by the dashed line, is used for the delamination analysis in Section. 4.3.3.

We performed nanoindentation tests to assess the hardness of the individual constituents in the ox-EBC. A total of 100 indents were made in 10×10 grid with indent spacing of 2 μm. We used a combination of optical imaging and the measured modulus (Section 2) to identify the indented phase. The hardness values of the Ni, glass, and $CeBO_3$ are 3, 1, and 10 GPa, respectively. Notably, the glass phase is softer than the metallic Ni phase, suggesting that localized plastic deformation in the inert glass phase may dissipate energy upon particle impact, preventing ignition of a reactive impacting particle. The nanoindentation hardness value of Ni indicates a much higher strength than that of coarse-grained commercially pure Ni in bulk form [34], assuming a typical hardness-to-strength ratio of 3 [35]. This discrepancy may be a result of the constraint of the ductile phase by the matrix or by interphase boundaries [31,36,37]. Indentation size and grain size effects may also contribute to this behavior [38].

Finally, we measured the CTE of the ox-EBC below the glass transition temperature using thermomechanical analysis in an inert Ar environment with a heating rate of 10 K/min. The temperature-averaged CTE of the monolithic glass-ceramic was 7×10^{-6} 1/K, which is lower than the CTE of Ni of 13.5×10^{-6} 1/K and is roughly 20% lower than that previously reported for a barium-aluminoborate glass with a similar composition [21]. This difference is likely due to the presence of $CeBO_3$ particles in the ox-EBC glass-ceramic phase which reduce the bulk CTE. Using these measured CTE values, we estimated the ox-EBC CTE over the full range of Ni compositions using the average of the Kerner-Schapery bounds. The estimated CTE of the ox-EBC with $V_{f,Ni} = 0.35$ is 10×10^{-6} 1/K. Note that this value is only slightly lower than that of typical Ni superalloy substrates (e.g., IN718 or Russian alloy EP741NP). For the ox-EBC/IN718 system at present, we note that the slight CTE mismatch results in compressive macroscale residual stresses in the ox-EBC during post-sinter cooling. This residual compressive stress suppresses through-thickness channel cracking as seen in the cross-section image in Fig. 3.

3. Modeling framework

To assess the delamination behaviors of the ox-EBC applied to a superalloy turbine blade of a reusable boost-stage oxygen-rich turbopump, we consider the idealized 1D configuration shown in Fig. 9, comprising a 100 μm-thick ox-EBC top coat, a 50 μm-thick pure Ni bond coat, and a 1 cm-thick IN718 substrate, symmetric about the substrate midplane.

Using this representative geometry, we assess the coating behavior during a nominal flight cycle of a reusable boost-stage rocket engine in which the engines are fired at four instances: takeoff, boost-back, re-entry, and landing. During each of these firings, the turbine is subjected to the following sequence of operating conditions:

i. *Startup*. The liquid oxygen (LOx) valve opens, allowing pure LOx to flow through the turbine at 90 K, the LOx saturation
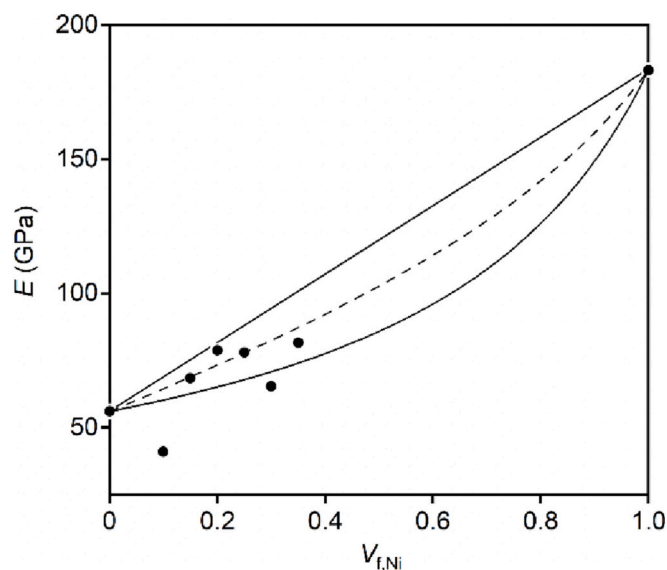

Fig. 8. Young's modulus of the ox-EBC (E_{ox}) vs. Ni volume fraction ($V_{f,Ni}$). The solid lines are the Hashin-Shtrikman bounds and the dashed line is their average.
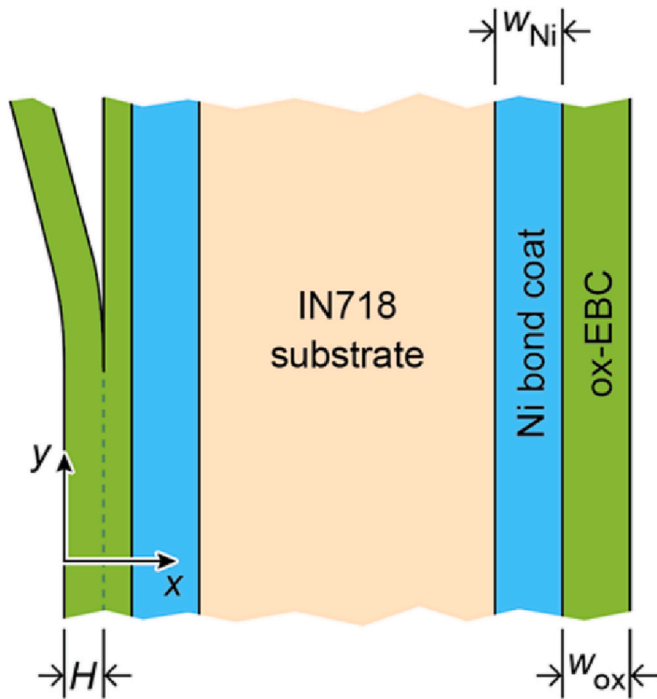
Fig. 9. Exemplary multilayer coating and underlying IN718 substrate. The blade is approximated as a flat symmetric substrate with a 1D temperature gradient through its thickness.

temperature at standard atmospheric pressure. The fuel valve opens after a brief delay, assumed here to be 150 ms [39].

ii. *Ignition.* The fuel valve opens, initiating combustion in the pre-burner and sending an oxygen-rich gaseous stream into the turbine. Here, we assume a steady-state gas temperature of 770 K which represents a typical turbine inlet temperature for oxidizer-rich staged combustion engines [2]. The oxygen-to-fuel mixture ratio is typically 40 to 60 [40], and the turbine inlet pressure is in the range of 150 to 600 bar [2,3].

iii. *Steady-state operation.* The oxygen-rich gaseous stream continuously flows through the turbine.

iv. *Throttle-down.* To prepare for shutdown, the fuel mass flow rate is reduced over several seconds, reducing the turbine inlet temperature. Here, we assume that the gas temperature reduces from 770 K to 420 K over 3 s.

v. *Shutdown.* The fuel valve is closed, and the LOx valve is closed 150 ms thereafter [39]. The turbopump is purged with inert gas to remove any residual propellants.

Considering this flight cycle, we discuss in Sections 3.1 and 3.2 the thermal and mechanical frameworks which underlie the thermo-mechanical analysis given in Section 4.

3.1. Thermal analysis

The temperature profile in the coated blade is calculated using the 1D heat equation,

$$\rho C_p \frac{\partial T}{\partial t} = k \frac{\partial^2 T}{\partial x^2}, \tag{1}$$

where T is temperature, ρC_p is volumetric heat capacity, and k is thermal conductivity, with surface normal direction x defined by the coordinate system given in Fig. 9. The layer interfaces are assumed to be perfectly bonded with no thermal resistance. To obtain a temperature history for the assumed flight cycle, we solve Eq. (1) numerically with the following

approach, outlined further in previous work [16].

We assume that the initial temperature of the blade is 300 K. Upon startup, the temperature evolves according to environment-dependent convective boundary conditions at the free surface, given by

$$q = h[T_s - T_\infty], \tag{2}$$

where q and T_s are the heat flux and the temperature at the free surface, respectively; h is the heat transfer coefficient; and T_∞ is the bulk temperature of the medium in contact with the coating.

During startup and shutdown, when LOx flows through the turbine, the heat transfer coefficient h depends strongly on the difference in temperature between the LOx and the coating. If the temperature difference is greater than 40 K, the LOx will boil and form a continuous film of O_2 vapor on the coating. Heat transfer then occurs via conduction through the vapor film with h of 130 W/m²-K [41]. If the temperature difference is less than 20 K, LOx boils without forming a continuous vapor film in a process termed nucleate boiling [41]. Here, h depends on the temperature difference between LOx and the coating and ranges from 500 to 15,000 W/m²-K in the temperature difference range 1.5 to 17 K [41]. If the temperature difference is sufficiently small or the hydrostatic pressure is sufficiently high, then LOx does not boil and h can be estimated using the correlation for external turbulent flows, given by

$$Nu = 0.0296(Re)^{0.8}(Pr)^{0.33}, \tag{3}$$

where Nu is the Nusselt number, defined as $Nu = \frac{hL}{k}$; Re is the Reynolds number, which is in the range of 10^5 to 10^6 due to the high liquid oxygen velocities in an oxygen-rich turbopump; and Pr is the Prandtl number, which is between 1 and 3 for LOx at a temperature of 90 K and pressures of 1 to 400 bar [42]. For simplicity, we assume $Pr = 2$. Inserting in Eq. (3) gives values of Nu from 400 to 2400. The thermal conductivity k of LOx varies slightly with pressure, increasing from 0.151 W/m-K to 0.187 W/m-K over the pressure range 1 to 600 bar [42]; here, we set $k = 0.17$ W/m-K. Assuming a characteristic dimension of the turbine blade L of 1 cm [43,44], the heat transfer coefficient h in the case of a small temperature difference is thus estimated between 7 and 41 kW/m²-K.

During ignition, steady-state operation, and throttle-down, when the oxygen-rich gaseous stream flows into the turbine, we assume that the heat transfer coefficient of the gaseous oxygen-rich stream h_{GOx} is 5×10^4 to 4×10^5 W/m²-K, which is the range of heat transfer coefficients for fuel-rich flow in the turbines of fuel turbopumps [45]. Finally, we assume no heat transfer ($h = 0$) between engine firings.

3.2. Mechanical analysis

We can estimate the steady-state energy release rate of an edge crack, represented by G, propagating parallel to the interface at an arbitrary depth H (Fig. 9) using

$$G(H) = U_t - U_l(H) - U_r(H), \tag{4}$$

where U_t is the elastic energy stored in the system far ahead of the crack tip, and U_l and U_r are the energy stored on the left and right side of the crack, respectively, far behind the crack tip. U_t, U_l, and U_r are given by

$$U_t = \int_0^w \frac{1}{2E} \left[\sigma_{yy}^2 + \sigma_{zz}^2 - 2\nu\sigma_{yy}\sigma_{zz} \right] dx, \tag{5}$$

$$U_l(H) = \int_0^H \frac{1}{2E} \left[\sigma_{yy}^2 + \sigma_{zz}^2 - 2\nu\sigma_{yy}\sigma_{zz} \right] dx, \tag{6}$$

and

$$U_r(H) = \int_H^w \frac{1}{2E} \left[\sigma_{yy}^2 + \sigma_{zz}^2 - 2\nu\sigma_{yy}\sigma_{zz} \right] dx, \tag{7}$$

respectively, and w is the total thickness of the coated blade. We

estimate the spatial distribution of stresses within the coated system, σ_{yy} and σ_{zz}, using beam theory, starting with

$$\sigma_{yy}(x) = \bar{E}(\epsilon_0 - \kappa x - \bar{c}\theta(x)), \tag{8}$$

where σ_{yy} is the normal stress in the y-direction; $\bar{E}$ is the effective plane-strain elastic modulus given by $\bar{E} = \frac{E}{1-\nu^2}$; ϵ_0 is the total strain in the system at $x = 0$; κ is the curvature about the z-axis; $\bar{c}$ is constant at $\bar{c} = (1 + \nu)$ due to plane-strain assumptions (i.e., $\epsilon_{zz} = 0$); and θ is the uni-axial thermal strain given by $\theta = \alpha(x)(T(x) - T_0)$, where α is the coefficient of thermal expansion and T_0 is the temperature at which the system is stress-free. Given the CTE values of the ox-EBC, Ni bond coat, and IN718 are comparable, we assume that the residual stresses post-sintering are negligible. Thus, we assume $T_0 = 300$ K for each layer within the coated blade. Note that the unknown values ϵ_0 and κ in Eq. (8) depend on the integral being computed. For instance, to calculate σ_{yy} that goes into the integral in Eq. (7) for U_r, unknowns ϵ_0 and κ are obtained by applying the force and moment balance equations on the part of the beam that lies between the integration limits used in Eq. (7), given as

$$\int_H^w \sigma_{yy} dx = 0 \tag{9}$$

and

$$\int_H^w x\sigma_{yy} dx = 0. \tag{10}$$

Having solved for ϵ_0 and κ, we then calculate σ_{yy} using Eq. (8) and subsequently calculate the normal stress-component in the z-direction, σ_{zz}, as

$$\sigma_{zz}(x) = \nu\sigma_{yy}(x) - E\theta(x). \tag{11}$$

We insert together these values for σ_{yy} and σ_{zz} into Eqs. (5)–(7) to then calculate G via Eq. (4). Further details of this procedure can be found in [16]. Note that there are typographical errors in the expression for out-of-plane stress (σ_{zz}) in [16], which we have corrected in Eq. (11).

We also use these stress values to gain insight into the dominant cracking mode during thermal transients by calculating the phase angle ψ for a delamination crack at the ox-EBC/Ni interface, where $\psi = 0°$ indicates mode I cracking and $\psi = 90°$ indicates mode II cracking. ψ is calculated using [46]

$$\tan\psi = \frac{K_{II}}{K_I} = \frac{Pw_{ox}\tan\omega - 2\sqrt{3}M}{Pw_{ox} + 2\sqrt{3}M\tan\omega}, \tag{12}$$

where K_I and K_{II} are the mode I and mode II stress intensity factors, respectively; P and M are the resultant force and moment in the ox-EBC far away from the crack-tip, respectively; and ω is the phase factor, which generally depends on the first and second Dundurs parameters α_D and β_D. For the ox-EBC/Ni interface, the second Dundurs parameter $\beta_D = 0.1$ based on the data given in Table 2; assuming that $\beta_D = 0$ for simplicity, ω depends only on α_D, which can be approximated as

$$\alpha_D = \frac{\bar{E}_{ox} - \bar{E}_R}{\bar{E}_{ox} + \bar{E}_R} \tag{13}$$

where $\bar{E}_{ox}$ is the plane-strain modulus of the ox-EBC and $\bar{E}_R$ is the effective modulus of the material beneath a single coating layer in Fig. 9

(i.e., Ni bond coat, IN718, Ni bond coat, ox-EBC). Since the elastic properties of Ni and IN718 are roughly equivalent and the substrate thickness is approximately 100 times greater than that of the coating, we approximate $\bar{E}_R \approx \bar{E}_{Ni} = \bar{E}_{IN718}$, giving $\alpha_D = -0.42$ and $\omega = 49°$ [46]. In Section 4, we use this phase angle prediction framework together with the results from the thermomechanical analysis to predict the evolution of fracture behavior.

For the following sections, we use the thermomechanical properties summarized in Table 2 unless otherwise specified. The ox-EBC properties correspond to a Ni volume fraction of 0.35, which corresponds to the lowest Ni content found to exhibit a percolating structure.

4. Model predictions and discussion

4.1. Overview of thermomechanical behavior during flight cycle

Here, we analyze the thermomechanical behavior of the coated turbine during a flight cycle of a reusable Falcon 9 booster, where the engines fire at four instances: takeoff, boostback, re-entry, and landing. The timing of each stage is summarized in Table 3. Because each hot fire lasts significantly longer than the through-thickness heat transfer timescale of the coated blade ($w_{sub}^2/4D = 8.5$ s), the blade attains a uniform steady-state temperature during engine operation and the precise duration of each hot fire has a negligible effect on the predicted energy release rate. We also assume the maximum values for the heat transfer coefficients, with $h_{GOx} = 4 \times 10^5$ W/m^2-K and $h_{LOx} = 41$ kW/m^2-K, which gives a conservative estimate of the energy release rate.

Fig. 10 shows the time evolution of the temperature at the free surfaces of the ox-EBC, $T_s = T_{x=0,w}$, during flight. Each hot fire results in a similar thermal cycle as governed by the operation sequence described in Section 3. For each hot fire, the surface temperature of the coated blade begins at an initial temperature that depends on the stage of flight. Next, the temperature drops to cryogenic temperatures. Ignition then increases the bulk fluid temperature and the heat transfer coefficient, causing the temperature to approach the steady-state turbine inlet temperature of 770 K over 10 s. This surface temperature remains constant until throttle-down, when the turbine inlet temperature (T_{GOx}) and T_s both decrease to 423 K over 3 s. The LOx flush during shutdown briefly reduces T_s to a minimum value which depends on the LOx heat transfer coefficient while the bulk of the blade remains at a higher temperature. The turbine is then purged to remove residual LOx. Heat conduction from the bulk of the blade to the cold surface, i.e., thermal soakback, continues until the coated blade achieves a spatially uniform temperature of 573 K.

4.1.1. Engine startup

We next consider in detail the thermomechanical behavior of the coated blade during engine startup at takeoff. The timescale of the LOx flush at startup ($t_{LOx} = 150$ ms) is longer than the heat diffusion timescale of the ox-EBC ($w_{ox}^2/D_{ox} = 5$ ms) but shorter than that of the blade substrate ($w_{sub}^2/4D = 8.5$ s). Thus, while the temperatures within the ox-EBC and the Ni bond coat drop to average values of 147 K and 160 K during this LOx flush, respectively, the bulk of the substrate remains at the ambient temperature, as shown in Fig. 11. Following this LOx flush, ignition raises the average temperature of the ox-EBC by 571 K in 110 ms, subjecting it to a hot shock, while the temperature of the midplane of the thick substrate does not increase until $t \approx 1$ s. A uniform steady state

Table 2
Thermal and mechanical material properties used for delamination analysis.

Layer	ρC_p (MJ/m^3-K)	k (W/m-K)	E (GPa)	ν	α (1/K $\times 10^{-6}$)
IN718 [47]	3.9	11.4	205	0.3	13
Ni bond coat [34]	3.9	70.4	205	0.3	12.6
ox-EBC top coat	4	7.7	83	0.3	9.9

Table 3
Timings of engine firing stages in a reusable booster stage flight.

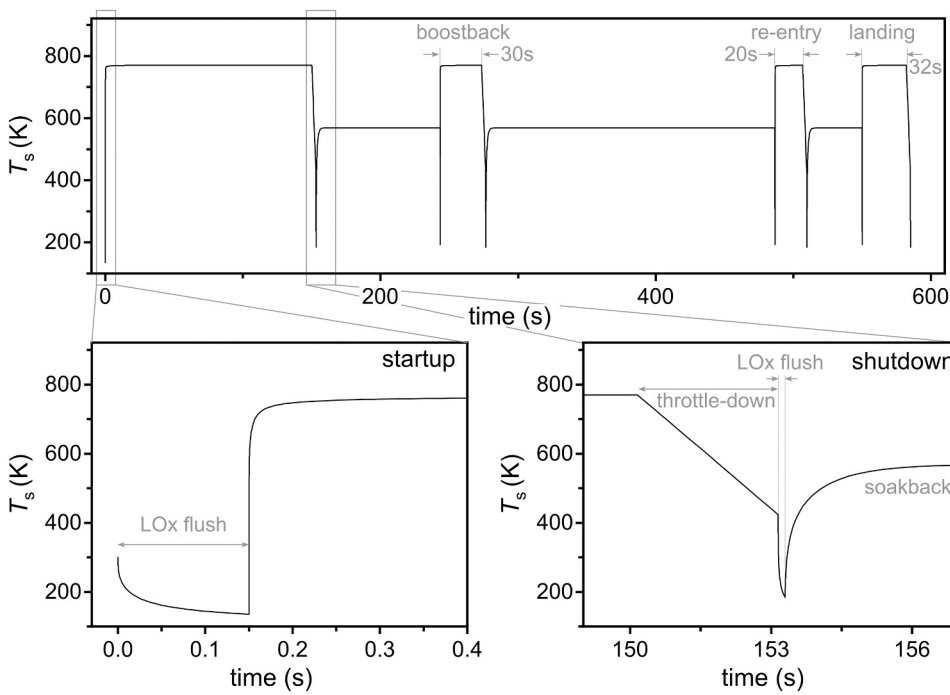| Firing stage	Delay after previous firing (s)	Duration (s)
Takeoff	–	150
Boostback	90	30
Re-entry	210	20
Landing	40	32

Fig. 10. Surface temperature of the coated blade (T_s) during a flight cycle for a reusable boost-stage engine. Engines are fired at four instances, with each firing resulting in a similar thermal cycle. The blade experiences a thermal transient during the startup and the shutdown for each of these cycles. At startup, a LOx flush followed by a hot oxygen-rich stream flow causes a hot shock. At shutdown, throttle-down and LOx flush result in a drastic temperature drop from the steady-state hot firing temperature of $T_s = 770$ K, resulting in a cold shock. We use $w_{ox} = 100$ μm, $w_{Ni} = 50$ μm, $w_{sub} = 1$ cm, $h_{GOx} = 4 \times 10^5$ W/m²-K, $h_{LOx} = 41$ kW/m²-K, and $t_{LOx} = 150$ ms.
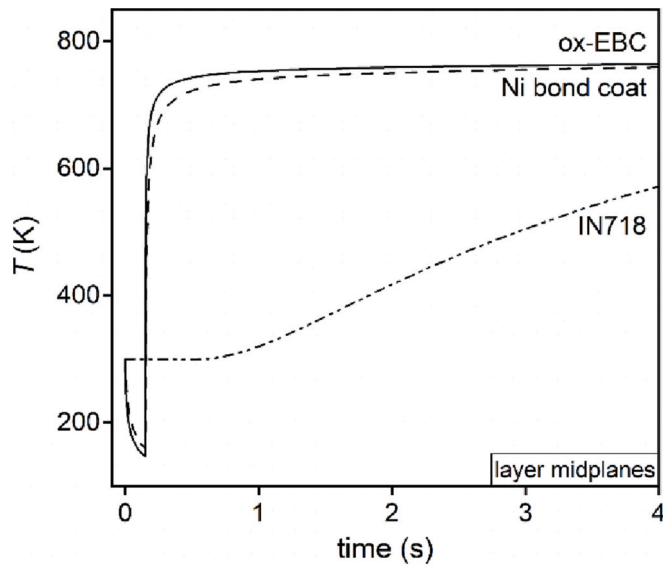
Fig. 11. Temperature (T) at the midplane locations in the ox-EBC ($x = 50$ μm), Ni bond coat ($x = 125$ μm), and IN718 substrate ($x = 5.2$ mm) during engine startup.
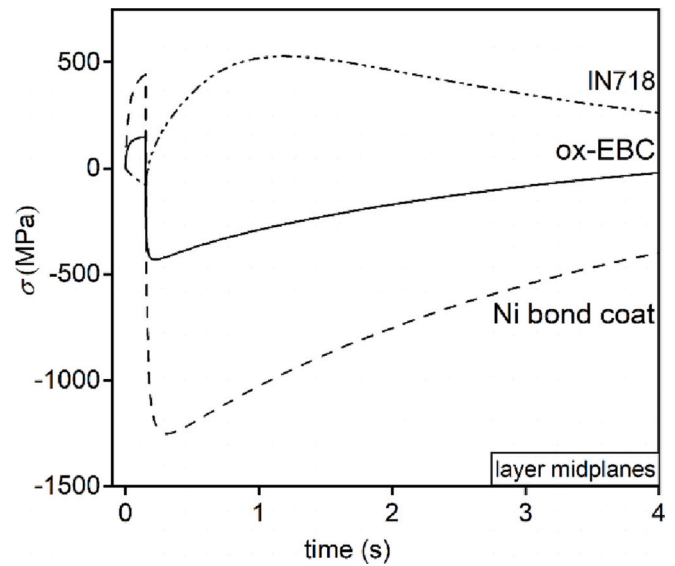

Fig. 12. Predicted stress ($\sigma = \sigma_{yy}$) at the midplanes of the ox-EBC, Ni bond coat, and IN718 substrate during engine startup.

of $T = 770$ K is achieved at $t \approx 20$ s.

Fig. 12 shows the resulting evolution of thermal stresses at the midplane locations of the ox-EBC ($x = 50$ μm), Ni bond coat ($x = 125$ μm), and IN718 substrate ($x = 5.2$ mm). The LOx flush at startup forms in-plane tensile stresses in the ox-EBC and the Ni bond coat, given that these layers experience lower temperatures than the thick IN718 substrate. The average tensile stresses peak at the end of the LOx flush, reaching maximum values of $\sigma_{ox} = 153$ MPa in the ox-EBC and $\sigma_{Ni} = 442$ MPa in the Ni bond coat, where the greater stress in the Ni bond coat is due to its larger Young's modulus (Table 2). A stress reversal occurs at ignition as the coating is heated while being constrained by a cold substrate. This hot shock leads to maximum average layer stress magnitudes at $t = 0.23$ s with $\sigma_{ox} = -431$ MPa and $\sigma_{Ni} = -1252$ MPa. Note

that these stress magnitudes are greater than those predicted for the preceding LOx flush. This difference results from a higher surface heat flux during ignition given larger values of heat transfer coefficient h and temperature difference T_s - T_∞. As shown in Fig. 12, the stresses approach their steady-state values as the heat diffuses into the bulk of the substrate, with steady-state stresses roughly an order of magnitude less than the peak stresses predicted for the thermal transient.

Fig. 13a shows the time evolution of G for edge delamination at both the ox-EBC midplane and the ox-EBC/Ni bond coat interface. Given that the substrate is much thicker than the ox-EBC, G is roughly given as $\frac{\sigma_{avg}^2 H}{2E}$, where H is the crack depth and σ_{avg} is the average stress in the delaminated part of the ox-EBC (with $0 < x < H$) prior to delamination, given by
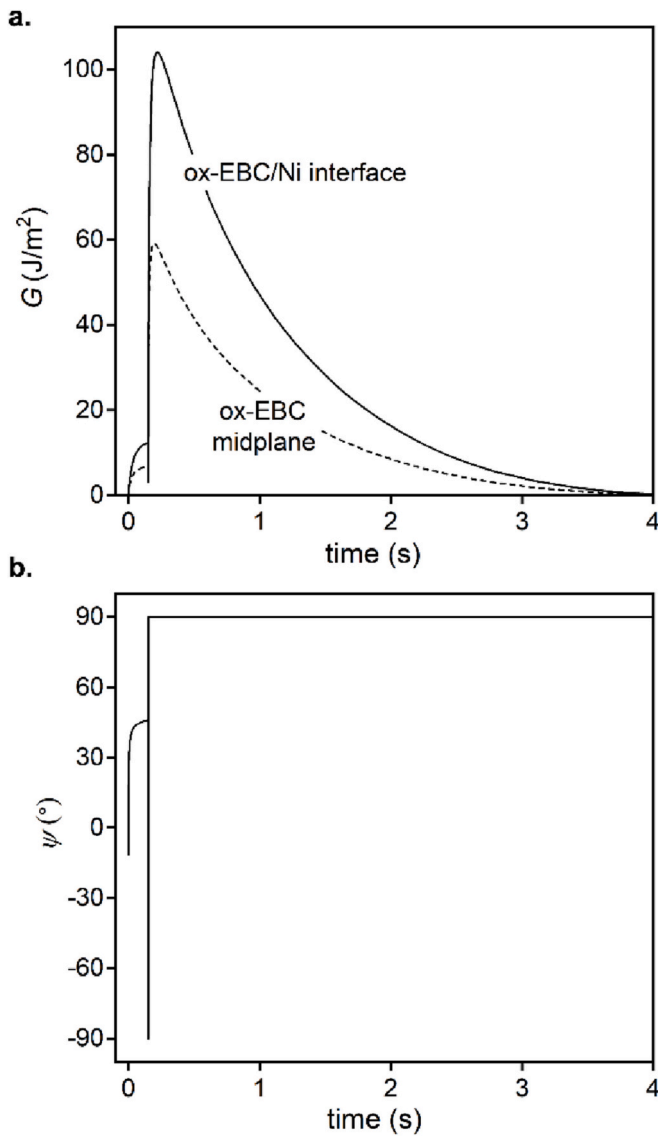
Fig. 13. (a) Energy release rate G at two different locations in the ox-EBC. (b) Evolution of phase angle at the ox-EBC/Ni interface during engine startup.

$$\sigma_{\text{avg}} = \frac{1}{H}\int_0^H \sigma_{yy}dx. \tag{14}$$

Since the Biot number $Bi = \frac{hw_{ox}}{k_{ox}}$ for the ox-EBC is always of order unity (with $Bi = 0.5$ for the LOx flow and $Bi = 5$ for the gaseous flow), the variation in σ_{yy} with respect to position x is negligible. As a result, σ_{avg} is independent of H, G increases linearly with H as shown in Fig. 13a, and G is maximum at the ox-EBC/Ni interface ($H = 100$ μm) at any time. We predict that G at the ox-EBC/Ni interface is 12 J/m² during the LOx flush at startup and increases to 103 J/m² during hot shock at ignition. For $t \gg w_{\text{sub}}^2/4D = 8.5$ s, G drops to a steady-state value of 15 J/m².

As discussed in Section 3.2, we can use the phase angle evolution within the ox-EBC to predict dominant fracture modes. The resulting phase angle evolution is shown in Fig. 13b. At the beginning of the LOx flush, the stress state in the ox-EBC is such that $P, M > 0$ in Eq. (12), resulting in a low phase angle ($\psi = -11°$) and mode I-dominant fracture at the ox-EBC/Ni interface. As time progresses, the stresses in the coating become more uniform, reducing the magnitude of moment M. This decrease in M causes the phase angle to increase to $\psi = 45°$ at the end of the LOx flush, reducing the influence of mode I cracking. When ignition begins, the resulting stress state (i.e., $P, M < 0$) causes the mode I

component to become negative ($K_{\text{I}} < 0$) for cracks in the ox-EBC, resulting in crack closure where the crack propagates purely via mode II fracture (with $\psi = 90°$). During the following steady state at $T = 770$ K, a uniform tensile stress within the ox-EBC ($P > 0$, $M = 0$) results in a phase angle of $\psi = 48.9°$.

4.1.2. Engine shutdown

Another key thermal transient occurs at engine shutdown, where the surface temperature of the coated blade begins at a uniform steady-state value of 770 K and rapidly drops. Fig. 14a shows the temperature at the midplane locations of the ox-EBC, Ni bond coat, and the IN718 substrate during engine throttle-down and the subsequent LOx flush during shutdown. During throttle-down, the average temperature drops by 340 K in the ox-EBC while the substrate midplane temperature drops by only 70 K, as the time duration for throttle-down (3 s) is much shorter than the heat diffusion timescale of the substrate. The subsequent LOx flush dramatically increases the temperature difference that drives heat flow at the coated surface (e.g., T_s - T_∞ from Eq. (2)), amplifying cold shock. Stresses in the ox-EBC and the Ni bond coat, plotted in Fig. 14b, follow a similar trend, showing a gradual buildup during throttle-down and a sudden spike during the LOx flush to peak values of $\sigma_{\text{ox}} = 535$ MPa and $\sigma_{\text{Ni}} = 1291$ MPa. This transient is followed by thermal soakback, which
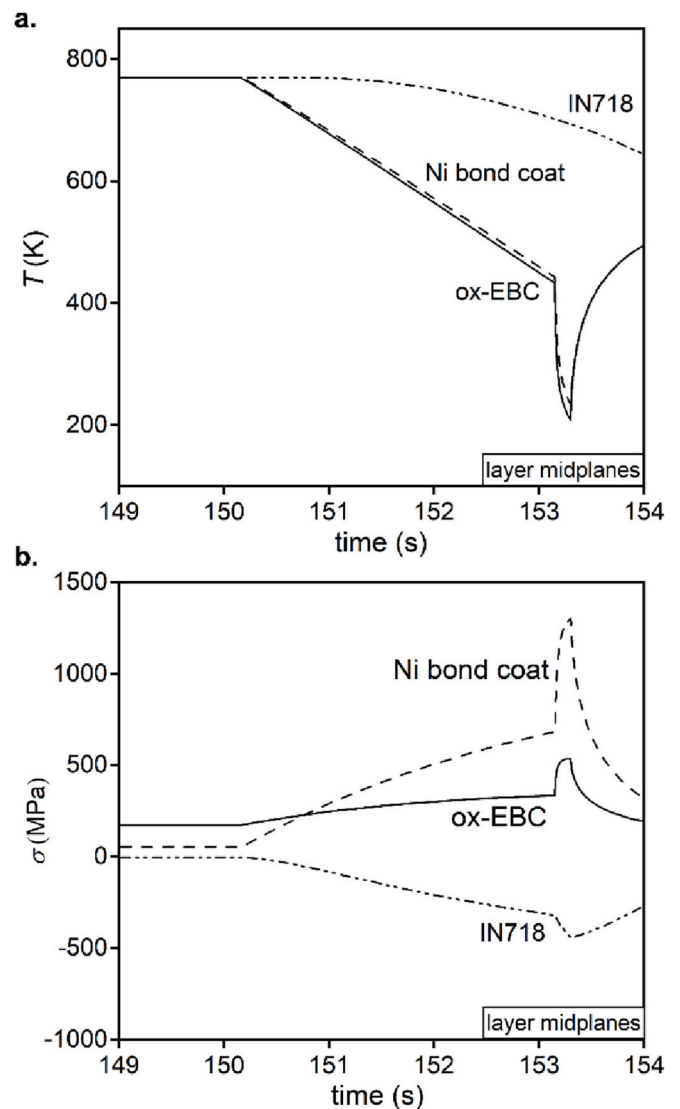

Fig. 14. (a) Temperature and (b) stress ($\sigma = \sigma_{yy}$) at the midplane locations of the ox-EBC, Ni bond coat, and IN718 substrate during engine shutdown.
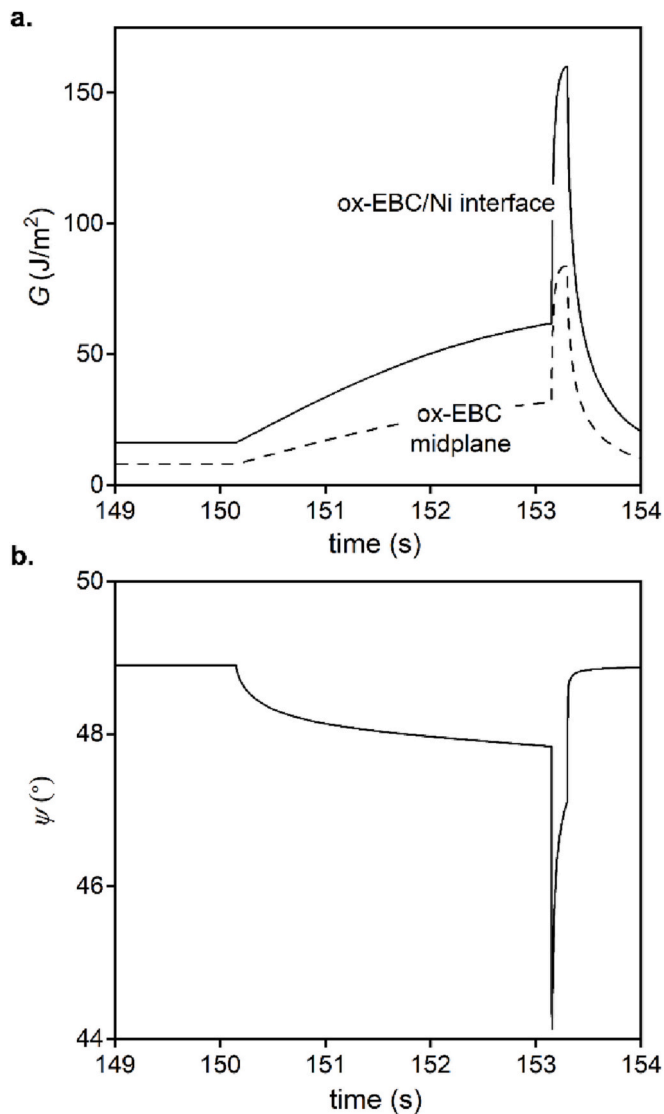
Fig. 15. (a) Energy release rate G at two different locations in the ox-EBC. (b) Phase angle ψ at the ox-EBC/Ni bond coat interface during engine shutdown.

establishes a steady-state temperature of 573 K within the blade after a time delay of order 10 s. The stresses during this steady state are an order of magnitude lower than those during the thermal transient.

Similar to the behavior under hot shock (Fig. 13a), the energy release rate for crack propagation increases monotonically with crack depth H as shown in Fig. 15a. The peak energy release rate for delamination at the ox-EBC/Ni interface is 160 J/m^2. The energy release rate later drops to 5 J/m^2 during the steady state following thermal soakback.

As discussed in the previous section, the stress state in the ox-EBC during the steady-state hot firing is such that $P > 0$, $M = 0$. Upon cold shock at engine shutdown, the stress state changes to P, $M > 0$. As a result, the phase angle for a crack at the ox-EBC/Ni interface decreases from 48.9° during the steady state to 47.8° as shown in Fig. 15b, slightly enhancing the mode I crack behavior. Next, the LOx flush further steepens the thermal gradient and resulting moment M, reducing the phase angle to 44°. During the steady state that follows thermal soak-back, the phase angle at the ox-EBC/Ni interface is $\psi = 48.9°$.

4.1.3. Overall behavior during a flight cycle

The coated blade is subjected to these thermal transients seen during startup and shutdown a total of four times during a flight cycle: at takeoff, boostback, re-entry, and landing. As discussed in Section 4.1.1,

the hot shock at startup causes compressive stresses in the coating. For boostback, re-entry, and landing, startup occurs with the bulk of the blade at an elevated temperature ($T_{sub} = 573$ K) due to the previous firing, whereas T_{sub} is 300 K for startup at takeoff. Thus, the peak compressive stress during takeoff ($\sigma_{ox} = -431$ MPa) is larger than that seen during subsequent firings ($\sigma_{ox} = -100$ MPa). Furthermore, we observe a higher tensile stress during cold shock at shutdown ($\sigma_{ox} = 535$ MPa) than during startup ($\sigma_{ox} = 439$ MPa) because the bulk of the blade is at a higher temperature post-ignition ($T_{sub} = 770$ K) than post-idling ($T_{sub} = 573$ K). Thus, hot shock at takeoff and cold shock at shutdown result in the highest energy release rate for ox-EBC delamination during a flight cycle. In particular, the cold shock at shutdown results in a higher energy release rate (160 J/m^2) than the hot shock at startup (103 J/m^2). The peak tensile stress during cold shock is greater than the peak compressive stress during hot shock because the CTE mismatch, with $\alpha_{ox} < \alpha_{sub}$, introduces a tensile stress in the ox-EBC during steady-state hot firing that enhances the tensile stresses that develop during the cold shock at shutdown. Furthermore, the hot shock delamination occurs purely under mode II ($\psi = 90°$), while the cold shock cracks are subjected to mixed-mode loading ($\psi \approx 45°$). Because interface mode II toughness is typically greater than interface mode I toughness [16], the ox-EBC is more susceptible to edge delamination due to the cold shock at shutdown.

For both hot shock and cold shock, the peak stresses in the ox-EBC exceed the typical strength value of Ni reported in literature [34]. As a result, effects such as plastic deformation and microcracking may strongly influence the delamination behavior, potentially giving rise to strain ratcheting under repeated thermal shocks or lowering the energy release rate below that predicted by a linear-elastic analysis [13,14]. We will address these phenomena and their implications on ox-EBC delamination in future work.

4.2. Effect of operating conditions

As discussed in the previous section, the risk for edge delamination in the ox-EBC is greatest during the LOx flush at shutdown. One way to reduce peak energy release rate is by modifying operating conditions. Here, we examine the variation of energy release rate with respect to LOx flush duration (t_{LOx}) and LOx heat transfer coefficient (h_{LOx}). The results in Fig. 16 show that for $h_{LOx} < 4000$ W/m^2-K, the peak energy release rate is independent of both t_{LOx} and h_{LOx}. This independence arises from the temperature uniformity within the coated blade at low Bi values which reduces the thermal stresses that arise from temperature gradients and thus the overall energy release rate. Under these conditions, the energy release rate is highest at the end of throttle-down. For $Bi \gg 1$, the temperature varies with position in the blade. In this case, increasing h_{LOx} increases the maximum temperature difference between the ox-EBC and the thick substrate ($T_{sub} - T_{ox}$), thus increasing the energy release rate. Note that the Fourier number of the substrate, $Fo_{sub}^{LOx} = 4D_{sub}t_{LOx}/w_{sub}^2$, is much less than unity over the entire range of t_{LOx}, indicating that transient effects dominate. Under these conditions, increasing t_{LOx} increases ($T_{sub} - T_{ox}$), thus increasing the energy release rate until $t_{LOx} \gg w_{ox}^2/D_{ox}$ (i.e., $Fo_{ox}^{LOx} \gg 1$) when the energy release rate asymptotes to a value governed by Bi. In this regime of $Fo_{ox}^{LOx} \gg 1$ and $Bi \gg 1$, further increase in h_{LOx} drive T_{ox} towards T_{LOx}, ultimately causing the energy release rate to reach a limiting value of 221 J/m^2.

Fig. 16 suggests two approaches to modifying operating conditions to mitigate the severity of the cold shock and lower the peak energy release rate. The first is to minimize the duration of the LOx flush, though the relatively flat energy release rate iso-contours suggest there is marginal benefit to changing the current valve timing on the order of 100 ms. The second and potentially more useful approach is to reduce the heat transfer coefficient by promoting nucleate or film boiling. In the present system, the temperature difference between the free surface of the coated blade and the LOx is always greater than 330 K, which, following
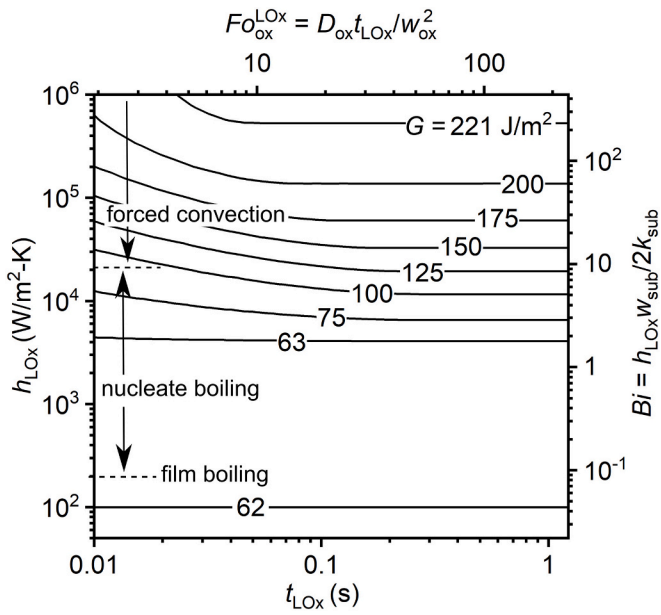
Fig. 16. Iso-contours of maximum energy release rate (G) during cold shock at shutdown with varying LOx flush duration (t_{LOx}) and heat transfer coefficient between LOx and the coated blade (h_{LOx}).

the discussion in Section 3.1, will cause film boiling under atmospheric pressure. However, under the extreme pressures in an oxygen-rich turbopump, greater temperature differences may be required to drive film boiling. These greater temperature differences may be reached by actively heating the turbine while the turbopump is idling. Although active thermal management is common practice in modern aeroengines, we are not aware of its use in rocket engine turbopumps, indicating an avenue for further development. The potential impact is great considering the interest in reusable launch vehicles, where active thermal management provides ancillary benefits such as mitigating thermal fatigue of bulk hardware.
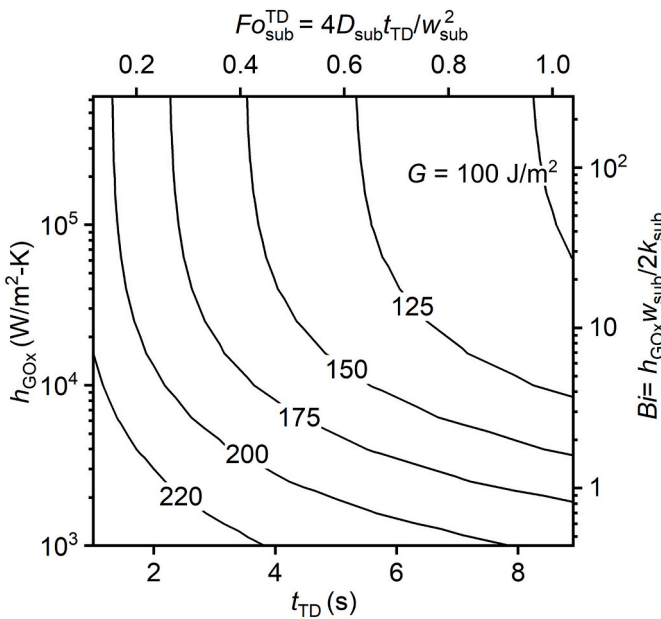

Fig. 17. Iso-contours of maximum energy release rate (G) during cold shock at shutdown with varying throttle-down duration (t_{TD}) and heat transfer coefficient between GOx and the coated blade (h_{GOx}).

Another strategy to minimize the peak energy release rate at engine shutdown is to tailor throttle-down parameters preceding the LOx flush. Fig. 17 shows the variation of G with respect to the throttle-down duration (t_{TD}) and the heat transfer coefficient between the flowing gas and the coated blade (h_{GOx}). The results demonstrate that with low Bi, an increase in h_{GOx} decreases the peak energy release rate. This decrease results from enhanced convective heat-transfer which decreases the substrate temperature at the end of throttle-down (T_{sub}), reducing the temperature difference between the coating and the substrate during the subsequent LOx flush ($T_{sub} - T_{ox}$), and ultimately reducing the energy release rate. For $Bi \gg 1$, the energy release rate is independent of Bi. In this regime, T_{sub} is limited by conduction and is therefore governed by the Fourier number. Note that the Fourier number of the throttle-down with respect to heat transfer through the substrate ($Fo_{sub}^{TD} = 4D_{sub}t_{TD}/w_{sub}^2$) increases from 0.12 to 1.05 as t_{TD} increases from 1 s to 9 s, indicating that the system is nearly isothermal. Under these conditions, an increase in t_{TD} (or Fo_{sub}^{TD}) decreases T_{sub} until $t_{TD} > w_{sub}^2/4D_{sub}$ ($Fo_{sub}^{TD} > 1$). In the regime of $Bi \gg 1$ and $Fo_{sub}^{TD} > 1$, T_{sub} approaches its lowest value of 420 K (Fig. 10), driving the energy release rate to the minimum of 100 J/m^2.

These results indicate that with the present condition of $h_{GOx} = 10^5$ W/m^2-K ($Bi > 10$), an increase in h_{GOx} will decrease the energy release rate only marginally. They also show that an effort to mitigate hot shock delamination by reducing h_{GOx} will adversely make the ox-EBC more susceptible to cold-shock delamination. However, we see that increasing t_{TD}, i.e., implementing a slower throttle-down, can help mitigate cold-shock delamination. For instance, an increase in t_{TD} from its present value of 3 s to 6 s will reduce the maximum energy release rate by 30%.

4.3. Design of a delamination-resistant ox-EBC

4.3.1. Effect of ox-EBC thickness and thermal conductivity

While thick ox-EBCs offer strong protection against particle impact ignition, thicker coatings are generally susceptible to delamination [11,15,16]. Considering this trade-off, we studied the effect of ox-EBC thickness on energy release rate, focusing specifically on the two most severe thermal transients: hot shock at startup during takeoff and cold shock at shutdown.

The effect of ox-EBC thickness w_{ox} and thermal conductivity k_{ox} on the energy release rate are coupled since they together determine the heat diffusion timescale of the ox-EBC. In particular, the energy release rate is governed by the ratio of the time at which it reaches its maximum value (t^*) to the heat diffusion timescale in the ox-EBC (w_{ox}^2/D_{ox}). Iso-contours of this ratio are shown in Fig. 18a. At low values of this ratio, the stress within the ox-EBC is non-uniform and its average value increases with k_{ox} and decreases with w_{ox}. Thus, the energy release rate shows a non-linear increase with w_{ox} in this regime, as shown in Fig. 18b. However, when $D_{ox}t^*/w_{ox}^2 \gg 1$, the stress is uniform within the ox-EBC and is independent of both w_{ox} and k_{ox}. In this regime, the energy release rate increases linearly with w_{ox}.

Fig. 19 shows iso-contours of energy release rate G for cold shock at shutdown with respect to the ox-EBC thickness w_{ox} and thermal conductivity k_{ox}. In this case, the energy release rate is always maximum near the end of the LOx flush (from $t^* = 0.12$ s to 0.15 s), such that $D_{ox}t^*/w_{ox}^2 > 1$ for the entire range of w_{ox} and k_{ox}. Thus, the stress state within the ox-EBC is uniform and independent of w_{ox} and k_{ox}, and the energy release rate increases linearly with w_{ox}, as shown in Fig. 19. However, throttle-down effects cause the system to deviate from uniform stress at low thermal conductivity and large ox-EBC thickness. In this regime, the stress decreases with the timescale for diffusion (Fig. 17). Therefore, the stress decreases with k_{ox} and increases with w_{ox}, and we observe a non-linear dependence of energy release rate on w_{ox} in this regime.
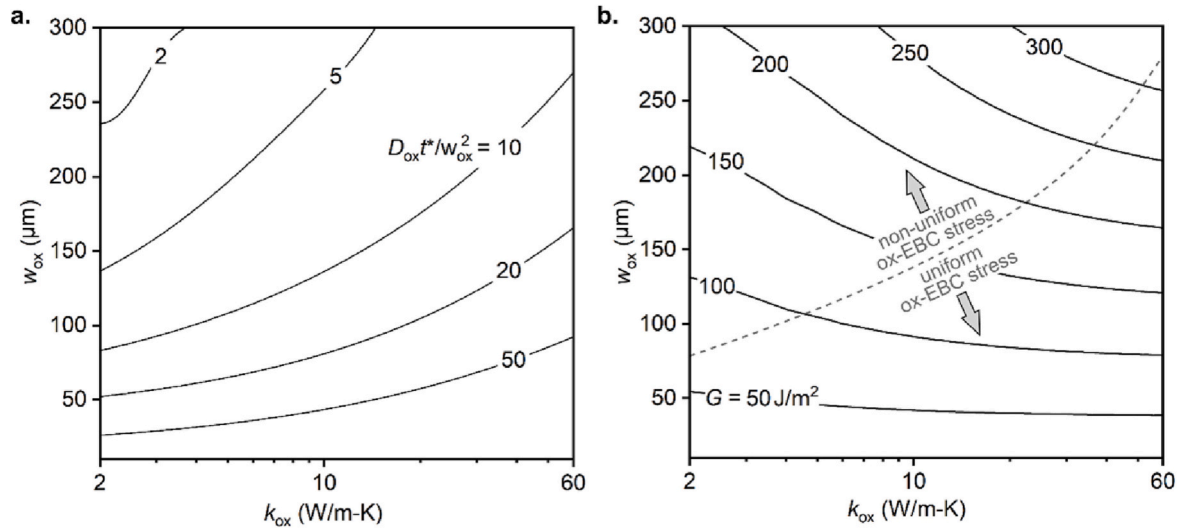
Fig. 18. (a) Iso-contours of $D_{ox}t^*/w_{ox}^2$ and (b) iso-contours of maximum energy release rate (G), both with varying ox-EBC thickness (w_{ox}) and ox-EBC thermal conductivity (k_{ox}) during hot shock at startup.
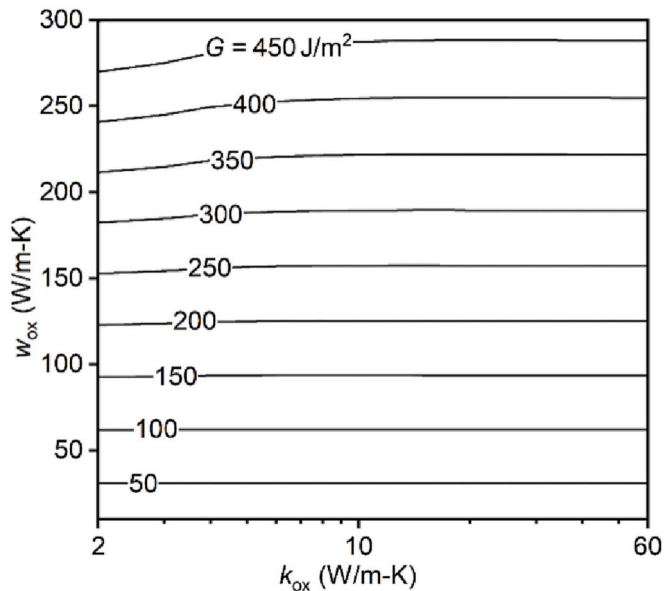

Fig. 19. Contours of maximum energy release rate (G) with varying ox-EBC thickness (w_{ox}) and ox-EBC thermal conductivity (k_{ox}) during cold shock at shutdown.

4.3.2. Optimal ox-EBC properties

In the ox-EBC system of present interest, the energy release rate during startup and shutdown increases with α_{ox} because the transient thermal stresses scale as $E_{ox}\alpha_{ox}(T_{ox} - T_{sub})$. However, the energy release rate at steady state is minimized when the CTE of the coating matches that of the substrate because the steady-state stresses scale as $E_{ox}(\alpha_{ox} - \alpha_{sub})(\Delta T_{sub})$. Thus, there exists an optimal ox-EBC CTE that can balance the transient and steady-state thermal stresses and minimize the peak energy release rate throughout the flight cycle. This effect is highlighted in Fig. 20a which shows the peak energy release rate from hot shock during take-off as a function of α_{ox} with all other parameters held fixed. Fig. 20a indicates that the optimal CTE depends on the thermal conductivity of the ox-EBC (k_{ox}) and decreases slightly from 7.8×10^{-6} 1/K to 7.0×10^{-6} 1/K as k_{ox} increases from the thermal conductivity of the monolithic glass-ceramic (2 W/m-K) to that of pure Ni (60 W/m-K). Fig. 20b shows the effect of α_{ox} on the peak energy release rate during cold shock, further highlighting the balance between transient and

steady-state thermal stresses. In this case, the optimal CTE remains near 4.5×10^{-6} 1/K over the full range of k_{ox} values.

While hot shock and cold shock result in similar energy release rate values on the order of 100 J/m², recall from Section 4.1 that a delamination crack propagates under mixed-mode loading conditions during cold shock ($\psi = 44°$) and pure mode II during hot shock ($\psi = 90°$). Given that coating interfacial toughness is generally less for mode I than for mode II [46], we aim to minimize the energy release rate under cold shock by designing coatings with CTE near the optimal cold shock CTE of 4.5×10^{-6} 1/K. Note that this optimal value is roughly half that of the current ox-EBC with $V_{f,Ni} = 0.35$ of $\alpha_{ox} = 10^{-5}$ 1/K. One way to reduce the current ox-EBC CTE to the optimal value is to substitute the borate glass-ceramic for a silicate glass-ceramic with a CTE on the order of 10^{-7} 1/K [48], resulting in a CTE of roughly 5×10^{-6} K. This substitution would also increase T_g and thus the maximum service temperature of the ox-EBC, enabling higher turbine inlet temperatures.

4.3.3. Effect of Ni percolation

The ox-EBC will delaminate when the energy release rate for crack propagation G exceeds the ox-EBC toughness. The ductile Ni phase helps prevent delamination by toughening the ox-EBC, similar to ductile phase reinforcements within brittle-matrix composites [30–32,49]. For composites with a discontinuous ductile phase, crack deflection is the primary toughening mechanism [28,50]. Accordingly, we assume that below the Ni percolation threshold in the ox-EBC (i.e., $V_{f,Ni} < 0.29$), a crack at the ox-EBC/Ni interface will deflect around the ductile Ni particles into the brittle glass-ceramic phase. In this case, the effective toughness G_{IC} can be estimated as [30]

$$G_{IC} = G_{gc/Ni} \frac{\left(1 + 2V_{f,Ni}\right)^{\frac{1}{2}}}{1 - V_{f,Ni}^{\frac{1}{2}}} \tag{15}$$

where $G_{gc/Ni}$ is the toughness of the glass-ceramic/Ni interface. Here we assume $G_{gc/Ni} = 20$ J/m² based on toughness values of other glasses and glass-ceramics [51,52]. Note that the brittle $CeBO_3$ particles will also toughen the brittle glass phase via crack-bridging, debonding, and frictional dissipation [32], but with a much smaller contribution than the Ni particles.

On the other hand, when the Ni volume fraction is above the percolation threshold in the ox-EBC (i.e., $V_{f,Ni} > 0.29$), the ductile Ni phase forms a continuous network within the ox-EBC and across the interface with the Ni substrate. For composites with a continuous ductile phase, crack bridging is the primary toughening mechanism, which
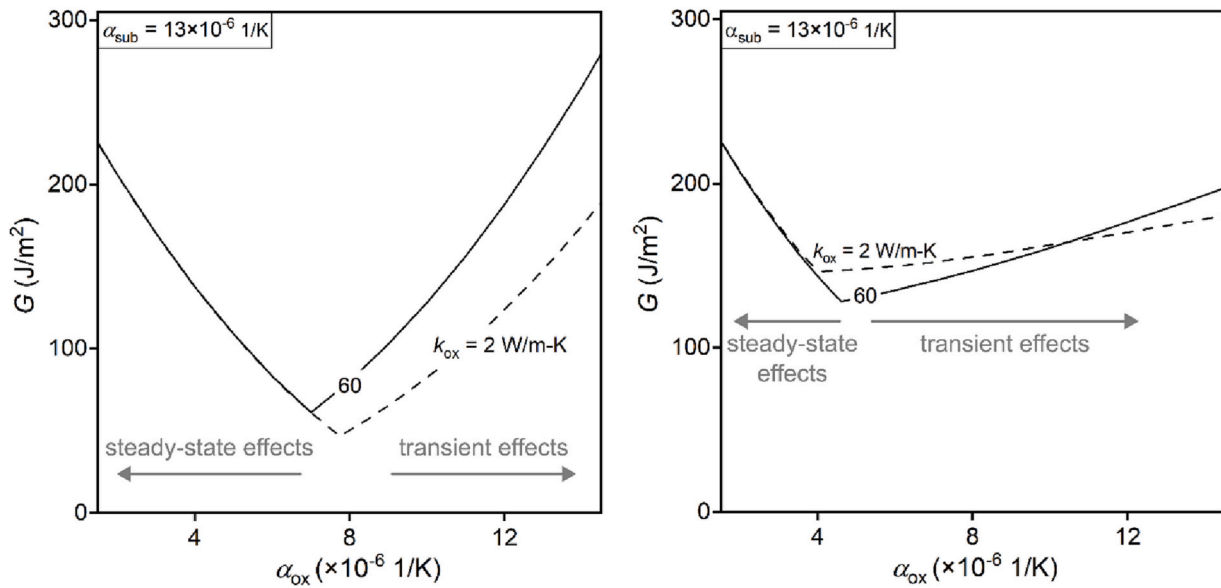
Fig. 20. Predicted peak energy release rate trade-off between (a) hot shock at startup and steady state at hot-firing as well as (b) cold shock at shutdown and steady-state at hot-firing, with respect to the ox-EBC CTE (α_{ox}).

offers greater improvements in toughness than crack deflection (Eq. (15)) [28,29,49]. The steady-state increase in toughness via crack bridging can be estimated as [31]

$$G_{IC} = G_{gc/Ni} + CV_{f,Ni}\sigma_0 a_0 \tag{16}$$

Here, C is a constant that ranges from 2 to 6 depending on the degree of constraint provided by the matrix, σ_0 is the mean flow strength of the ductile ligaments, and a_0 is the average ligament radius. For the present ox-EBC system, we assume for the Ni phase that $\sigma_0 = 150$ MPa [34] and $a_0 = 2$ μm (estimated from SEM micrographs). We further assume $C = 4$, which corresponds to the conditions of brittle-phase fracture and decohesion at the brittle/ductile phase interface [31], both of which are present in the current ox-EBC. Under these assumptions, Eq. (16) predicts that the percolating Ni structure increases the toughness of the ox-EBC by 420 J/m². This value is in line with toughness values of several metal/ceramic interpenetrating phase composites, including those of Al/Al$_2$O$_3$ with toughness 435 J/m² [33], Cu/Al$_2$O$_3$ with toughness 195 J/m² [53], Ni-NiAl/Al$_2$O$_3$ with toughness 369 J/m² [54], and Co/WC

alloys with toughness 475 J/m² [37].

To further examine the effects of the percolating Ni structure on the ox-EBC performance, we show in Fig. 21 the effect of Ni volume fraction ($V_{f,Ni}$) on peak G during cold shock at shutdown. To calculate the peak energy release rate, we assume that the variation of E_{ox} with $V_{f,Ni}$ is given by the average of the Hashin-Strikman bounds (Fig. 8), while the variation of α_{ox} with $V_{f,Ni}$ is given by the average of the Kerner-Schapery bounds. k_{ox} is assumed to follow the lower Hashin-Strikman bound below the percolation threshold ($V_{f,Ni} < 0.29$) and the upper Hashin-Strikman bound above the percolation threshold ($V_{f,Ni} > 0.29$). Recall from Section 4.1.3 that this energy release rate value corresponds to a crack subjected to mixed-mode loading ($\psi = 44°$). To obtain the effective energy release rate under pure mode I, we use [16]

$$G_I = \frac{G}{1 + \tan^2[(1-\lambda)\psi]} \tag{17}$$

where λ is an empirical parameter that varies between 0 and 1. We assume $\lambda = 0.5$, giving $G_I = 0.83G$.

The results are shown together in Fig. 21, where the solid curve represents the ox-EBC steady-state mode I toughness G_{IC}, which is governed by crack deflection below the percolation threshold and by crack bridging above the percolation threshold. For a given Ni volume fraction, the toughening increment due to crack bridging is nearly two orders of magnitude higher than that due to crack deflection. As a result, the ox-EBC toughness is higher than the crack-driving force only when the Ni volume fraction is above the percolation threshold, suggesting that the percolating Ni structure and its toughening contributions are critical for mitigating delamination in service. Additionally, if we consider the risk of particle impact ignition, Ni is more prone to ignition than the inert glass-ceramic phase. Thus, the optimal ox-EBC for mitigating particle impact ignition contains a low Ni volume fraction. Taken together, we predict that the optimal Ni volume fraction in this class of ox-EBCs is slightly higher than the percolation threshold, likely in the range of 0.29 to 0.35. Such coatings could resist delamination under a wide range of LOx flow conditions up to a critical coating thickness of roughly 200 μm (Figs. 16 and 19).

5. Conclusions

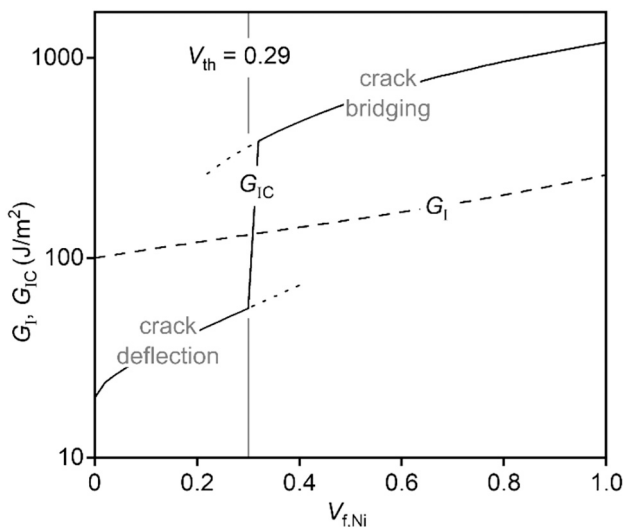We have assessed the delamination risk of a composite oxygen-

Fig. 21. Peak energy release rate for delamination (G_I) and toughness (G_{IC}) of the ox-EBC versus Ni volume fraction ($V_{f,Ni}$).

compatible environmental barrier coating (ox-EBC) that can protect against particle impact ignition in the oxygen-rich environments of reusable staged-combustion rocket engines. Structural characterization experiments showed that the coating, which comprises Ni and a glass-ceramic, forms an interpenetrating composite structure above a Ni volume fraction of 0.3. This Ni volume fraction is an excellent agreement with the theoretical percolation threshold for penetrable spheres.

By combining heat transfer analysis with linear elastic fracture mechanics, we analyzed the temperatures, thermal stresses, and energy release rates that develop in the coating under a nominal flight cycle of a reusable boost-stage rocket engine. The ox-EBC is most susceptible to delamination during cold shock upon engine shutdown, where the energy release rate is 160 J/m^2 for the delamination of a 100 μm-thick ox-EBC. Our analysis shows the energy release rate can be reduced by modifying operating conditions; e.g., we find that active thermal management – namely, preheating the turbine to promote film boiling – can reduce the energy release rate to a minimum of 60 J/m^2. Another way to reduce the energy release rate is through material design; our parametric study reveals that within the relevant ox-EBC thermal conductivity range, the energy release rate scales linearly with ox-EBC thickness and is minimized when the CTE of the ox-EBC is 4.5×10^{-6} 1/K.

Estimates of the toughening increment due to Ni highlight the important role of percolation in mitigating delamination of brittle coatings. Below the Ni percolation threshold ($V_{f,Ni} < 0.29$), the Ni phase is discontinuous and enhances toughness via crack deflection. The resulting predicted ox-EBC toughness is on the order of 50 J/m^2. By contrast, above the percolation threshold, the Ni phase percolates throughout the ox-EBC and enhances toughness via crack bridging. The resulting predicted ox-EBC toughness is 440 J/m^2. Thus, considering the peak energy release rate of 160 J/m^2 during thermal cycling, a percolating Ni structure is required to prevent ox-EBC delamination during the flight cycle of a reusable staged-combustion rocket engine.

We acknowledge that these predicted toughness mechanisms and ox-EBC toughness values require experimental validation. We also note that in this work, we do not consider plastic deformation of the ductile Ni phase which is likely to result from thermal stresses in the ox-EBC before or during debonding [13,14]. Previous works show that plastic deformation greatly reduces energy release rate in ductile phase-reinforced brittle-matrix composites [55], and the percolating ductile-phase architecture of the ox-EBC warrants a similar analysis. Given the repeated thermal cycling and extended lifetimes of components in reusable rocket engines, we also aim to explore the fatigue behavior of the ox-EBC in future work. Several studies indicate that the fracture toughness of bulk composites degrade under fatigue loading [49,56]; however, analogous studies on composite coatings are sparse. Our forthcoming work will address these research gaps.

CRediT authorship contribution statement

Isha Gupta: Investigation, Methodology, Visualization, Writing – original draft. **Spencer V. Taylor:** Investigation, Methodology, Writing – original draft. **Christopher M. Kiel:** Investigation, Methodology. **Andres Garcia-Jimenez:** Investigation, Methodology. **Zachary C. Cordero:** Conceptualization, Supervision, Writing – review & editing.

Declaration of competing interest

The authors declare that they have no known competing financial interests or personal relationships that could have appeared to influence the work reported in this paper.

Data availability

Data will be made available on request.

References

[1] M. Crofton, J. Emdee, E. Petersen, M. Micci, Particle impact ignition in high pressure oxygen: initial results, Jt. Propuls. Conf. Amp Exhib. 46 (2010) 7134–7145, https://doi.org/10.2514/6.2010-7134.

[2] H. Mårtensson, S. Andersson, S. Trollheden, S. Brodin, Rocket Engines: Turbomachinery, 2008.

[3] L. Schoenman, Selection of burn-resistant materials for oxygen-driven turbopumps, J. Propuls. Power 3 (1987) 46–55, https://doi.org/10.2514/3.22951.

[4] L. Shao, G. Xie, C. Zhang, X. Liu, W. Lu, G. He, J. Huang, Combustion of metals in oxygen-enriched atmospheres, Metals 10 (2020) 128, https://doi.org/10.3390/met10010128.

[5] W. Knuth, R. Crawford, Oxygen-rich combustion process applications and benefits, Jt. Propuls. Conf. 27 (1991) 1–8, https://doi.org/10.2514/6.1991-2042.

[6] Frank J. Benz, J.M. Homa, R.C. Shaw, Burn Propagation Rates of Metals and Alloys in Gaseous Oxygen, ASTM International, 1986.

[7] J.A. Nesbitt, Thermal modeling of various thermal barrier coatings in a high heat flux rocket engine, Surf. Coat. Technol. 130 (2000) 141–151, https://doi.org/10.1016/S0257-8972(00)00723-4.

[8] D. Greuel, O. Haidn, K. Fritscher, Thermal barrier coating for cryogenic rocket engines, Jt. Propuls. Conf. Amp Exhib. 38 (2002) 4145–4156, https://doi.org/10.2514/6.2002-4145.

[9] Z. Xue, A.G. Evans, J.W. Hutchinson, Delamination susceptibility of coatings under high thermal flux, J. Appl. Mech. 76 (2009) 1–7, https://doi.org/10.1115/1.3086590.

[10] J. Robertson, M.I. Manning, Limits to adherence of oxide scales, Mater. Sci. Technol. 6 (1990) 81–92, https://doi.org/10.1179/mst.1990.6.1.81.

[11] J.W. Hutchinson, A.G. Evans, On the delamination of thermal barrier coatings in a thermal gradient, Surf. Coat. Technol. 149 (2002) 179–184, https://doi.org/10.1016/S0257-8972(01)01451-7.

[12] A.G. Evans, J.W. Hutchinson, The mechanics of coating delamination in thermal gradients, Surf. Coat. Technol. 201 (2007) 7905–7916, https://doi.org/10.1016/j.surfcoat.2007.03.029.

[13] M.R. Begley, H.N.G. Wadley, Delamination of ceramic coatings with embedded metal layers, J. Am. Ceram. Soc. 94 (2011) s96–s103, https://doi.org/10.1111/j.1551-2916.2011.04438.x.

[14] M.R. Begley, H.N.G. Wadley, Delamination resistance of thermal barrier coatings containing embedded ductile layers, Acta Mater. 60 (2012) 2497–2508, https://doi.org/10.1016/j.actamat.2011.12.039.

[15] S. Sundaram, D.M. Lipkin, C.A. Johnson, J.W. Hutchinson, The influence of transient thermal gradients and substrate constraint on delamination of thermal barrier coatings, J. Appl. Mech. 80 (2013) 1–13, https://doi.org/10.1115/1.4007727.

[16] R.W. Jackson, M.R. Begley, Critical cooling rates to avoid transient-driven cracking in thermal barrier coating (TBC) systems, Int. J. Solids Struct. 51 (2014) 1364–1374, https://doi.org/10.1016/j.ijsolstr.2013.12.029.

[17] A.F. Atlanova, G.A. Babaeva, E.A. Belov, D.I. Dubovik, J.A. Pestov, M.E. Judina, L.V. Cherkasov, V.I. Semenov, F.J. Chelkis, A.M. Kashkarov, K.P. Khaplanov, Compound for producing a metal-ceramic coating, US6090191A. https://patents.google.com/patent/US6090191A/en, 2000 (accessed November 28, 2022).

[18] Atlanova Aza Fyodorovna, Drozdova Yulia Viktorovna, Ivshin Nikolay Aleksandrovich, Korovkin Andrey Viktorovich, Development of Ceramic Coating to Protect Turbine Gas Train, 2019 (accessed November 28, 2022), https://elibrary.ru/item.asp?id=43845892.

[19] SpaceX CRS-6 Mission. https://www.nasa.gov/sites/default/files/files/SpaceX_NASA_CRS-6_PressKit.pdf, 2015 (accessed November 28, 2022).

[20] J.F. MacDowell, Aluminoborate glass-ceramics with low thermal expansivity, J. Am. Ceram. Soc. 73 (1990) 2287–2292, https://doi.org/10.1111/j.1151-2916.1990.tb07590.x.

[21] V.P. Klyuev, B.Z. Pevzner, Composition dependence of thermal expansion and glass transition temperature for barium aluminoborate glasses, Glas. Phys. Chem. 27 (2001) 54–61.

[22] G.N. Carneiro, H. Vargas, J.A. Sampaio, Thermo-optical and structural properties of barium aluminoborate glasses, J. Alloys Compd. 777 (2019) 1327–1333, https://doi.org/10.1016/j.jallcom.2018.11.044.

[23] P. Pernice, S. Esposito, A. Aronne, V.N. Sigaev, Structure and crystallization behavior of glasses in the BaO–B2O3–Al2O3 system, J. Non-Cryst. Solids 258 (1999) 1–10, https://doi.org/10.1016/S0022-3093(99)00554-2.

[24] S.W. Haan, R. Zwanzig, Series expansions in a continuum percolation problem, J. Phys. Math. Gen. 10 (1977) 1547–1555, https://doi.org/10.1088/0305-4470/10/9/013.

[25] M.D. Rintoul, S. Torquato, Precise determination of the critical threshold and exponents in a three-dimensional continuum percolation model, J. Phys. Math. Gen. 30 (1997) L585–L592, https://doi.org/10.1088/0305-4470/30/16/005.

[26] Salvatore Torquato, H.W. Haslach Jr., Random Heterogeneous Materials: Microstructure and Macroscopic Properties, Springer-Verlag, New York, 2002.

[27] S. Torquato, F. Lado, Effective properties of two-phase disordered composite media: II. Evaluation of bounds on the conductivity and bulk modulus of dispersions of impenetrable spheres, Phys. Rev. B 33 (1986) 6428–6435, https://doi.org/10.1103/PhysRevB.33.6428.

[28] P.A. Trusty, J.A. Yeomans, The toughening of alumina with iron: effects of iron distribution on fracture toughness, J. Eur. Ceram. Soc. 17 (1997) 495–504, https://doi.org/10.1016/S0955-2219(96)00099-4.

[29] L.D. Wegner, L.J. Gibson, The fracture toughness behaviour of interpenetrating phase composites, Int. J. Mech. Sci. 43 (2001) 1771–1791, https://doi.org/10.1016/S0020-7403(01)00016-9.

[30] M.F. Ashby, Criteria for selecting the components of composites, Acta Metall. Mater. 41 (1993) 1313–1335, https://doi.org/10.1016/0956-7151(93)90242-K.

[31] M.F. Ashby, F.J. Blunt, M. Bannister, Flow characteristics of highly constrained metal wires, Acta Metall. 37 (1989) 1847–1857, https://doi.org/10.1016/0001-6160(89)90069-2.

[32] A.G. Evans, Perspective on the development of high-toughness ceramics, J. Am. Ceram. Soc. 73 (1990) 187–206, https://doi.org/10.1111/j.1151-2916.1990.tb06493.x.

[33] H. Prielipp, M. Knechtel, N. Claussen, S.K. Streiffer, H. Müllejans, M. Rühle, J. Rödel, Strength and fracture toughness of aluminum/alumina composites with interpenetrating networks, Mater. Sci. Eng. A 197 (1995) 19–30, https://doi.org/10.1016/0921-5093(94)09771-2.

[34] Ansys Granta, Materials Information Management. https://www.ansys.com/products/materials (accessed November 28, 2022).

[35] D. Tabor, The Hardness of Metals, Oxford University Press, United Kingdom, 1951.

[36] J.J. Roa, E. Jiménez-Piqué, J.M. Tarragó, D.A. Sandoval, A. Mateo, J. Fair, L. Llanes, Hall-Petch strengthening of the constrained metallic binder in WC–Co cemented carbides: experimental assessment by means of massive nanoindentation and statistical analysis, Mater. Sci. Eng.: A 676 (2016) 487–491, https://doi.org/10.1016/j.msea.2016.09.020.

[37] L.S. Sigl, H.F. Fischmeister, On the fracture toughness of cemented carbides, Acta Metall. 36 (1988) 887–897, https://doi.org/10.1016/0001-6160(88)90143-5.

[38] R.A. Mirshams, P. Parakala, Nanoindentation of nanocrystalline Ni with geometrically different indenters, Mater. Sci. Eng. A 372 (2004) 252–260, https://doi.org/10.1016/j.msea.2004.01.010.

[39] S.H. Kang, I. Moon, S.Y. Lee, Experiments on an oxidizer-rich preburner for staged combustion cycle rocket engines, J. Propuls. Power 30 (2014) 1098–1103, https://doi.org/10.2514/1.B35202.

[40] J. Hulka, J. Forde, R. Werling, V. Anisimov, V. Kozlov, I. Kositsin, Modification and verification testing of a Russian NK-33 rocket engine for reusable and restartable applications, Jt. Propuls. Conf. Exhib. 34 (1998) 1–26, https://doi.org/10.2514/6.1998-3361.

[41] E.G. Brentari, Patricia J. Giarratano, Boiling Heat Transfer for Oxygen, Nitrogen, Hydrogen, and Helium, US National Bureau of Standards, 1965.

[42] EES, Engineering Equation Solver | F-Chart Software: Engineering Software. https://fchartsoftware.com/ees/ (accessed November 28, 2022).

[43] A. Abdul-Aziz, in: Structural Evaluation of a Space Shuttle Main Engine (SSME) High Pressure Fuel Turbopump Turbine Blade, NASA Contract Rep 198428, 1996, pp. 1–20.

[44] J.L. Boynton, R. Tabibzadeh, S.T. Hudson, Investigation of rotor blade roughness effects on turbine performance, J. Turbomach. 115 (1993) 614–620, https://doi.org/10.1115/1.2929298.

[45] A. Abdul-Aziz, M.T. Tong, A. Kaufman, Thermal finite-element analysis of space shuttle main engine turbine blade, Finite Elem. Anal. Des. 5 (1989) 337–348, https://doi.org/10.1016/0168-874X(89)90012-7.

[46] M.R. Begley, J.W. Hutchinson, The Mechanics and Reliability of Films, Multilayers and Coatings, Cambridge University Press, United Kingdom, 2017.

[47] https://www.matweb.com/search/datasheet.aspx?matguid=94950a2d209040a09b89952d45086134&cck=1, 1996 (accessed November 28, 2022).

[48] R. Roy, D.K. Agrawal, H.A. McKinstry, Very low thermal expansion coefficient materials, Annu. Rev. Mater. 19 (1989) 59–81, 0084-6600/89/0801-0059.

[49] K. Badrinarayanan, A.L. McKelvey, R.O. Ritchie, K.T. Venkateswara Rao, Fracture and fatigue-crack growth behavior in ductile-phase toughened molybdenum disilicide: effects of niobium wirevs particulate reinforcements, Metall. Mater. Trans. A 27 (1996) 3781–3792, https://doi.org/10.1007/BF02595627.

[50] V.V. Krstic, P.S. Nicholson, R.G. Hoagland, Toughening of glasses by metallic particles, J. Am. Ceram. Soc. 64 (1981) 499–504, https://doi.org/10.1111/j.1151-2916.1981.tb10313.x.

[51] J.J. Brennan, S.R. Nutt, SiC-whisker-reinforced glass-ceramic composites: interfaces and properties, J. Am. Ceram. Soc. 75 (1992) 1205–1216, https://doi.org/10.1111/j.1151-2916.1992.tb05559.x.

[52] R. Rogier, F. Pernot, Phosphate Glass-Ceramic-Titanium Composite Materials, Springer, Germany, 1991.

[53] N.A. Travitzky, Microstructure and mechanical properties of aluminarcopper composites fabricated by different infiltration techniques, Mater. Lett. 36 (1998) 114–117, https://doi.org/10.1016/S0167-577X(98)00012-3.

[54] J. Rödel, H. Prielipp, N. Claussen, M. Sternitzke, K.B. Alexander, P.F. Becher, J. H. Schneibel, Ni3AlAl2O3 composites with interpenetrating networks, Scr. Metall. Mater. 33 (1995) 843–848, https://doi.org/10.1016/0956-716X(95)00301-B.

[55] H. Cai, G. Bao, Crack bridging in functionally graded coatings, Int. J. Solids Struct. 35 (1998) 701–717, https://doi.org/10.1016/S0020-7683(97)00082-6.

[56] L. Llanes, Y. Torres, M. Anglada, On the fatigue crack growth behavior of WC–Co cemented carbides: kinetics description, microstructural effects and fatigue sensitivity, Acta Mater. 50 (2002) 2381–2393, https://doi.org/10.1016/S1359-6454(02)00071-X.